Work Hardening, Dislocation Structure, and Load Partitioning in Lath Martensite Determined by In Situ Neutron Diffraction Line Profile Analysis

DOI:
10.1007/s11661-017-4172-0

Document Version
Accepted author manuscript

Published in:
Metallurgical and Materials Transactions A: Physical Metallurgy and Materials Science

TITLE:

Work Hardening, Dislocation Structure and Load Partitioning in Lath-Martensite Determined by *In Situ* Neutron Diffraction Line Profile Analysis

AUTHOR NAMES and AFFILIATIONS:

Stefanus Harjo[1], Takuro Kawasaki[1], Yo Tomota[2], Wu Gong[1], Kazuya Aizawa[1], Geza Tichy[3], Zengmin Shi[4] and Tamas Ungár[3,5]

[1]J-PARC Center, Japan Atomic Energy Agency, 2-4 Shirane Shirakata, Tokai-mura, Naka-gun, Ibaraki, 319-1195, Japan

[2]Graduate School of Science and Engineering, Ibaraki University, 4-12-1, Nakanarusawa, Hitachi, Ibaraki, 316-8511, Japan (Present address: Research Center for Structure Materials, National Institute for Materials Science, 1-2-1 Sengen, Tsukuba, Ibaraki 305-0047, Japan)

[3]Department of Materials Physics, Eötvös University, Budapest, PO Box 32, H-1518, Hungary

[4]College of Materials and Chemical Engineering, China Three Gorges University, 8 Daxue Rd, Xiling, Yichang, Hubei, China

[5]Materials Performance Centre, The University of Manchester, M13 9PL, Manchester, UK

CORRESPONDING AUTHOR:

Stefanus Harjo

Neutron Science Section, J-PARC Center, Japan Atomic Energy Agency

2-4 Shirane Shirakata, Tokai-mura, Naka-gun, Ibaraki, 319-1195, Japan

Email: stefanus.harjo@j-parc.jp

Tel: +81 29 2843266 Fax: +81 29 2843370

ABSTRACT

In situ neutron diffraction during tensile deformation of an as-quenched lath martensite steel containing 0.22 mass% of carbon, is performed using a high-resolution time-of-flight neutron diffractometer to clarify the large work-hardening behavior at the beginning of plastic deformation. The diffraction peaks at plastically deformed states exhibit asymmetries as the reflection of redistributions of the stress and dislocation densities/arrangements in lath-packets where the dislocation glides are favorable (soft packet) and unfavorable (hard packet). The dislocation density is as high as 10^{15} m^{-2} at the as-quenched state, and then during tensile straining, the load and the dislocation density become different between the two lath-packets. The dislocation character and arrangement vary also in the hard packet, but hardly change in the soft packet. In the hard packet, dislocations that are mainly of screw-type at the as-quenched state vary to be mainly of edge-type, and the random arrangement at the as-quenched state rearranges towards a dipole character or a highly correlated arrangement. The hard packet plays an important role in the high work hardening in martensite, which could be understood by taking into account not only the increase of the dislocation density but also the change in dislocation arrangement.

KEYWORDS:

Lath martensite; dislocation; work hardening; neutron diffraction; electron microscopy

1. Introduction

Lath martensite steel is one of the most widely used high strength structural materials. It is obtained by quenching to room temperature (RT) from a temperature where the austenitic phase is stable. Martensitic phase transformation produces a fine grain structure with extremely high dislocation density [1]. The microstructure of lath martensite typically comprises several packets with different crystallographic orientations in a prior austenite grain, where the packets are formed by blocks [2,3]. The blocks are subdivided into sub-blocks with the same variant, where the smallest constituents are plate-crystals called laths having the size of several tens of nm.

The elastic limit of lath martensite steel is relatively low [4], indicating that work hardening after yielding at the beginning of plastic deformation is very high. It was also reported that cold rolling increased the elastic limit substantially bringing higher 0.2% proof stress [4]. To make clear such an unusual deformation behavior, the changes in dislocation density (ρ) in the cold rolled and tensile deformed lath martensitic Fe–18Ni alloys were measured by X-ray diffraction (XRD) [4] and neutron diffraction (ND) [5] applying the classical Williamson-Hall (W-H) plot [6]. As a result, the ρ values were reported to decrease with plastic deformation, since the slopes in the classical W-H plots decreased with plastic deformation.

In general, the change of flow stress due to dislocations ($\Delta\sigma$) can be evaluated using the Taylor's equation [7]:

$$\Delta\sigma = \sigma - \sigma_0 = \alpha\, \mu\, M_T\, b\, \sqrt{\rho}\,, \qquad (1)$$

where σ is the flow stress due to dislocations, σ_0 is the sum of the friction stress of dislocations and the stress due to the effect solute element strengthening, α is a geometrical coefficient between zero to unity, μ is the shear modulus, M_T is the Taylor factor taking into account the effect of texture and b is the Burgers vector.

The value of the α coefficient is usually assumed to be unchanged during deformation, and hence the increase in the $\Delta\sigma$ value is caused solely by the increase in the value of ρ, unless the grain size is very small. Therefore, the decrease in the ρ value in lath martensitic Fe–18Ni alloy, reported in [4,5], seems to be puzzling. This remains questionable despite that the high ρ value invoked by martensitic transformation can decrease slightly induced by plastic deformation, similarly as reported in [8]. Hutchingson et al. [9] carried out similar experiments but interpreted the slopes of classical W-H plots as residual intragranular shear stresses generated during martensitic

transformation. They claimed that the residual intragranular shear stresses were reduced in magnitude by plastic deformation, subsequently controlling the stress-strain behavior. However, their interpretation is questionable from the view point of diffraction profile analysis presenting in this paper.

In situ ND has been demonstrated to be a powerful tool for clarifying phenomena in various engineering applications [10-17]. We have reported *in situ* high-resolution ND experiments of an as-quenched lath martensite steel containing 0.22 mass% of carbon during tensile deformation [17]. We found that the initially homogeneous lath structure was disrupted by plastic tensile deformation, turning to produce a composite on the length scale of martensite lath packets. The diffraction patterns of plastically strained martensite steel revealed characteristically asymmetric peak profiles in the same way as has been observed in materials with heterogeneous dislocation structures [18,19]. The diffraction patterns were evaluated by the Convolutional Multiple Whole Profile (CMWP) procedure based on physically modeled profile functions for dislocations, crystallite size and planar defects [20,21]. Lath packets oriented favorably (soft-packet orientation components, SO) or unfavorably (hard-packet orientation components, HO) for dislocation glide became soft or hard, in which the dislocation density became smaller or larger compared to the initial average dislocation density. The decomposition into SO and HO was accompanied by load redistribution and the formation of long-range internal stresses between the two lath-packets.

In the present work, which is the second part of [17], the evolution of lattice strains and dislocation properties during tensile deformation will be presented and discussed in correlation with the composite behavior of the lath-packet structure. The average dislocation density values, provided by neutron line profile analysis, will be compared with the results obtained by scanning transmission electron microscopy (STEM) observation. The variations of dislocation character and dislocation arrangement during tensile deformation in the two lath packet types will be discussed in relation to the work hardening. The work-hardening mechanism of the lath martensite will be discussed by correlating the dislocation structure with the flow stress in the Taylor equation.

2. Experimental

The specimen preparation was almost identical with that in our previous paper (the first part) [17] and the chemical composition was Fe–0.22C–0.87Si–1.64Mn–0.024Ti–

0.0015B–0.0025N in mass% [22]. The averaged packet and block sizes were 20 and 4 μm, respectively. A rod-shaped specimen with a diameter of 5 mm and a length of 15 mm was prepared after austenitic solution treatment for *in situ* ND experiments during tensile test using TAKUMI [23], a high-resolution time-of-flight (TOF) neutron diffractometer for engineering sciences at the Materials and Life Science Experimental Facility of the Japan Proton Accelerator Research Complex.

Tensile deformation for *in situ* ND was performed in a stepwise manner with load control at the elastic region and in a continuous manner with a constant crosshead speed (the strain rate was 10^{-5} s^{-1}) at the plastic region. The strain was monitored by a strain gauge glued on the specimen. The deformations at the plastic region were increased step by step to arbitrary strains followed by unloading. The ND data collection was conducted continuously using an event-recording mode during tensile deformation. Further details of the ND conditions have been given in our previous paper [17]. Diffraction patterns related to the step load-holding states, plastic deformations, and unloaded states after plastic deformations were then extracted according to the macroscopic stress and strain data. The macroscopic stress and strain values relevant to the diffraction patterns were averaged over the interval times for data extraction. Figure 1 shows the macroscopic stress–strain curve of the specimen. The unloaded states remained in some plastic strains. The elastic limit was approximately 350 MPa, and therefore the rate of work hardening was extremely high. In the macroscopic stress–strain curve obtained from continuous loading under the same strain rate up until fracture, a very high tensile strength of approximately 1.65 GPa and a uniform strain of approximately 6.1% were confirmed.

Data analysis for evaluating lattice strain was performed using the Z-Rietveld software [24]. The analyses of dislocations were performed using the CMWP procedure on the diffraction profiles collected from the unloaded states after plastic deformation. Diffraction peak profiles of LaB_6 powder measured under the same conditions as the *in situ* ND measurements were used to determine the instrumental peak profiles for the dislocation analyses.

STEM observations were performed using an electron microscope, Tecnai G2F20 with STEM-BF (bright field) and STEM-ADF (annular dark field) modes operated at 200 kV. The thickness of the observation area in the TEM foil was estimated using the electron energy-loss spectroscopy (EELS) method [25], and the ρ value was determined

using the linear cross-sectioning method.

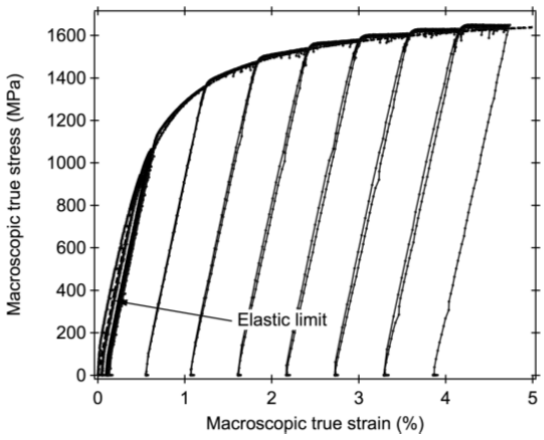

Figure 1 Macroscopic Stress-strain curve of as-quenched lath martensite steel in this study.

3. Results

3.1 Lattice strain

Figure 2 shows the observed and Rietveld-calculated neutron diffraction patterns before tensile deformation. The crystal structure used for martensite was BCC. The crystal structures of lath martensite steels with the carbon content of below 0.6 mass% were reported to be BCC at RT [26]. Although martensite in a Fe–30Ni–0.2C alloy was reported to have a BCT structure with the c/a ratio of about 1.02 [27], the sample used in this study was however Ni-free, and the martensite peaks in Figure 2 were perfectly fitted using the TAKUMI instrumental profile shape function with a BCC structure. Texture evaluated from the ratio of *hkl* peak integrated intensity was hardly observed before tensile deformation. A weak α fiber texture was formed after 4.7% tensile deformation.

Retained austenite (γ) was confirmed in the specimen, as shown in Figure 2, and its fraction before tensile deformation was refined to be approximately 3.7%. The lattice constants of martensite and γ were determined to be 0.28646(0) nm and 0.35912(3) nm, respectively. Figure 3 shows the fractions of γ measured at unloaded states after plastic tensile deformations. The γ still existed after 4.7% tensile deformation, but its fraction decreased to be approximately 2.2%. A small amount of γ might transform to martensite during plastic tensile deformation. The existence of γ was difficult to confirm on

microscopy images, probably due to the tiny size and/or the martensitic transformation during specimen preparation.

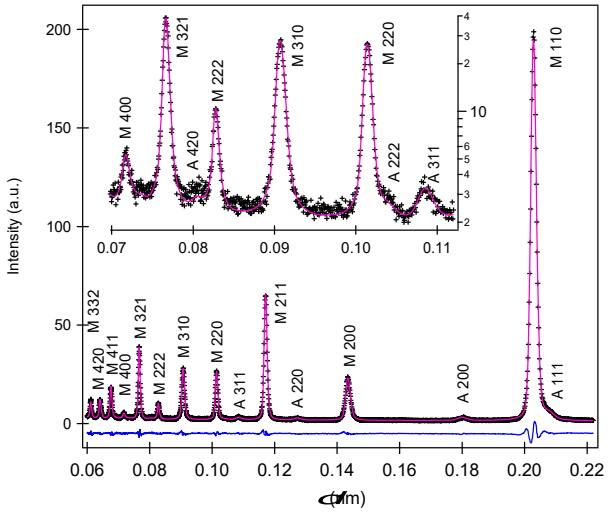

Figure 2 The observed (black-plus symbol) and Rietveld fitted (pink line) neutron diffraction profiles before tensile deformation, in which *d* is the lattice spacing. Blue line is the residual between the fitted and the observed profiles. The up-left figure is the enlarged profiles with log scale in the vertical axis for the *d* values of 0.07 to 0.112 (nm). M or A indicates martensite or retained austenite, respectively. (color for online only)

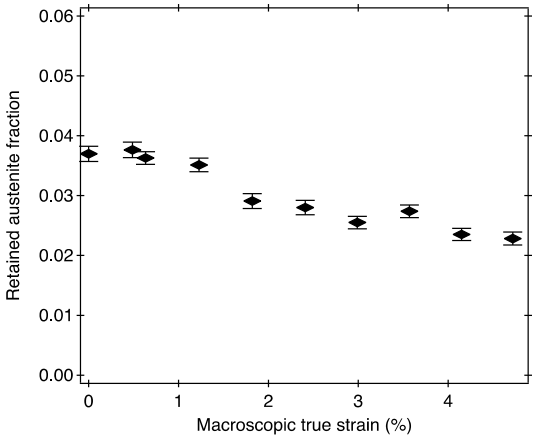

Figure 3 The fractions of retained austenite measured after plastic tensile deformations (at unloaded states). (color for online only)

The lattice strain can be evaluated from the peak shift according to the following

equation:

$$\varepsilon^{hkl} = (d^{hkl} - d_0^{hkl}) / d_0^{hkl} \quad (2)$$

where ε, d, and d_0 stand for the lattice strain, measured lattice spacing, and reference lattice spacing, respectively. The lattice spacing determined before tensile deformation was used as d_0. Figure 4 shows the lattice strains in the axial direction measured for martensite and γ. In Figure 4(a), all martensite-*hkl* lattice strain responses to the applied true stress deviated from their linearity to have smaller increasing rates. On the contrary, the γ <311> lattice strains at the related region had larger values than the martensite lattice strains. Note that the <311> lattice strain represents the bulky elastic strain for FCC polycrystalline materials [10,15]. In Figure 4(b), the residual lattice strain for martensite that were averaged over <*hkl*> decreased becoming compressive with increasing macroscopic strain, while that for γ increased becoming tensile oppositely. These results indicate that γ plays the role of the hard phase in the material used in this study. Similar behaviors have been observed in transformation-induced plasticity (TRIP)-aided multiphase steels [12,14], in which retained austenites, because of carbon enrichment, showed higher flow stress than the ferrite–bainite matrix. In the lath martensite steel used in this study, the carbon enrichment must be small and hence, this is not the case. Another similar behavior has been observed in Fe–Cu alloy [16], in which tiny copper precipitates behaved as the hard phase, in spite of the low flow stress at the elasto-plastic deformation in the case of copper polycrystalline aggregates [13]. Extremely small austenite particles embedded in the strong martensite matrix are speculated to possibly exhibit higher flow resistance as with tiny Cu particles in iron. The martensite lattice strain responses, however, are still maintained in the increasing tendency showing work hardening.

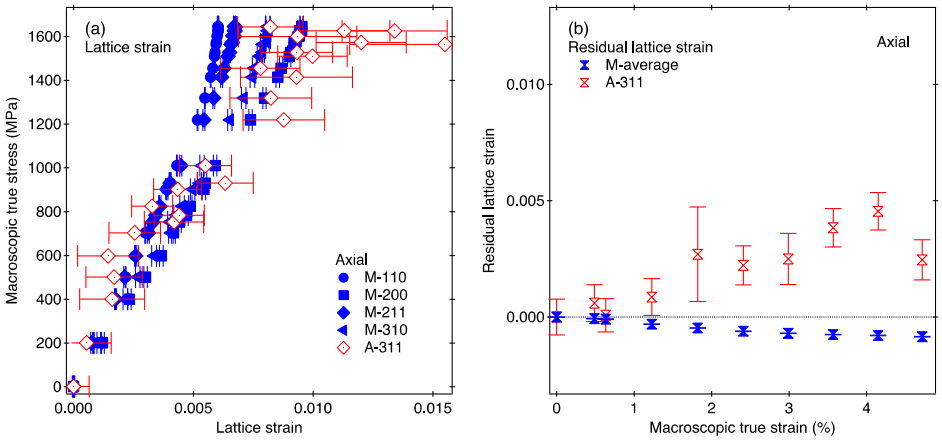

Figure 4 (a) Lattice strains measured during tensile deformation and (b) residual lattice strains measured at unloaded states after plastic tensile deformations in the axial direction. M or A indicates martensite or retained austenite, respectively. (color for online only)

3.2 Strain anisotropy and elastic anisotropy

The *hkl* dependent Young's modulus (E_{hkl}) values obtained from the lattice strain measurements are summarized in Table 1. The Young's modulus values in a cubic crystal must follow the linear relation [28]:

$$1/E_{hkl} = B + F\,H^2 , \qquad (3)$$

where B and F are constants and H^2 is the fourth order invariant of hkl, $H^2 = (h^2k^2 + h^2l^2 + k^2l^2) / (h^2 + k^2 + l^2)^2$. The inverse values of measured E_{hkl} are plotted versus H^2 in Figure 5. The figure showed that the relation in equation (3) is fulfilled perfectly within the experimental errors with $B = 0.0059$ and $F = -0.0062$. The B and F are related to the elastic constants (c_{11}, c_{12} and c_{44}) as [28]:

$$B = \frac{c_{11}+c_{12}}{(c_{11}+2c_{12})(c_{11}-c_{12})} , \quad F = \frac{1}{c_{44}} - \frac{2}{c_{11}-c_{12}} . \qquad (4)$$

Obviously, two numbers, *i.e.* B and F, are insufficient to provide three elastic constants without any further information. Fortunately, we know that the c_{44}/c_{12} ratio for metals is usually between 0.5 and 0.7 [29]. Taking $c_{44}/c_{12} = 0.6$, the values of B and F with equation (4) provided the elastic constants for the martensite investigated here:

$c_{11} = 283(5)$ GPa, $c_{12} = 161(4)$ GPa, $c_{44} = 97(4)$ GPa. (5)

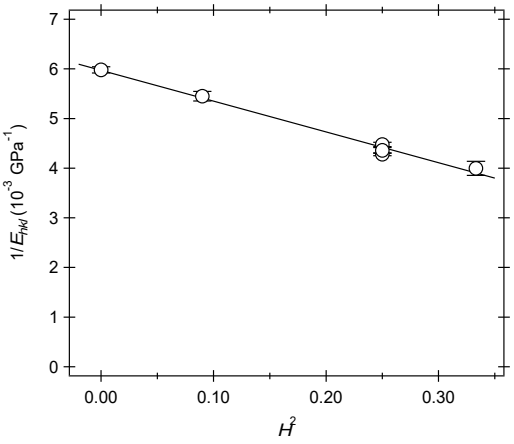

Figure 5 The measured $1/E_{hkl}$ values versus H^2.

With these elastic constant values the elastic anisotropy (A) of our martensite material was 1.59. The A value of α-Fe is 2.4 [30]. The A value of a martensite steel investigated in [30] was obtained to be 1.01. The compositions of the martensite investigated here and that reported in [30] are, however, different from each other. The major constituents of the present martensite steel are Fe–0.22C–0.87Si–1.64Mn–0.024Ti in mass%, whereas those reported in [30] are Fe–0.52C–0.22Si–1.0Mn–0.3Al in mass%. The A value of 1.59 is between the values of α-Fe and the martensite steel in [30]. This indicates only that the elastic anisotropy is rather sensitive to the composition and probably also to the exact quenching conditions of martensitic steel.

Strain anisotropy in line broadening means that the full width at half maximum (*FWHM*) values of diffraction peaks are not in a monotonous function of diffraction order [31]. Figure 6(a) shows the *FWHM* values for the martensite steel before deformation, the 0.6%, 3% and 4.7% tensile deformed states versus $K = 1/d$. The *FWHM* values were evaluated by a Gaussian function from the physical profiles of the diffraction peaks that are free from the instrumental effect, as provided by the CMWP procedure. The increase in the *FWHM* versus K indicates substantial microstrains caused by the large dislocation density. The apparent scatter of the *FWHM* values around the global ascending trend is typical for strain anisotropy. Strain anisotropy can be rectified by taking into account the *hkl* dependent dislocation contrast $C(hkl)$ [31]. In polycrystalline cubic materials $C(hkl)$ can be averaged over the permutations of *hkl*, and it can be written as [32]:

$$\bar{C} = \bar{C}_{h00}\left(1 - qH^2\right), \qquad (6)$$

where $\bar{C}_{h00}$ is the average contrast for the *h00* type reflections, q is a parameter depending on the dislocation character, e.g. screw or edge, and the elastic anisotropy of the material. It was shown in [31,33] that the weird, apparently irregular, behavior of the *FWHM* values in the conventional W-H plot, shown in Figure 6(a), was rectified when K was replaced by $K\sqrt{\bar{C}}$ in the modified W-H plot, shown in Figure 6(b), where q = 1.7 was used. According to a theoretical computation for BCC with a slip system of <111> {110}, elastic anisotropy of 1.6, and c_{12}/c_{44} of 0.6, the q value of 0.2 stands for edge type and 2.5 for screw type [33]. The q value used in Figure 6(b) is in between of 0.2 and 2.5, and therefore indicates that the dislocations have a mixed character of edge and screw with a larger proportion of screw-type. Figure 6(b) shows that the *FWHM* values follow a perfect straight line, substantiating the evaluation of the elastic constants and the value of q = 1.7. According to a TEM work in [34], a dislocated martensite structure consists of two kinds of dislocations; one is the straight screw dislocation that must be induced by lattice invariant shear, and the other is the tangled dislocation that must be inherited from the austenite matrix. The tangled dislocations are generated in the matrix to relax the internal stress caused by transformation strains. This TEM work supports the obtained q value, that dislocations in as-quenched martensite have a mixed character of screw and edge.

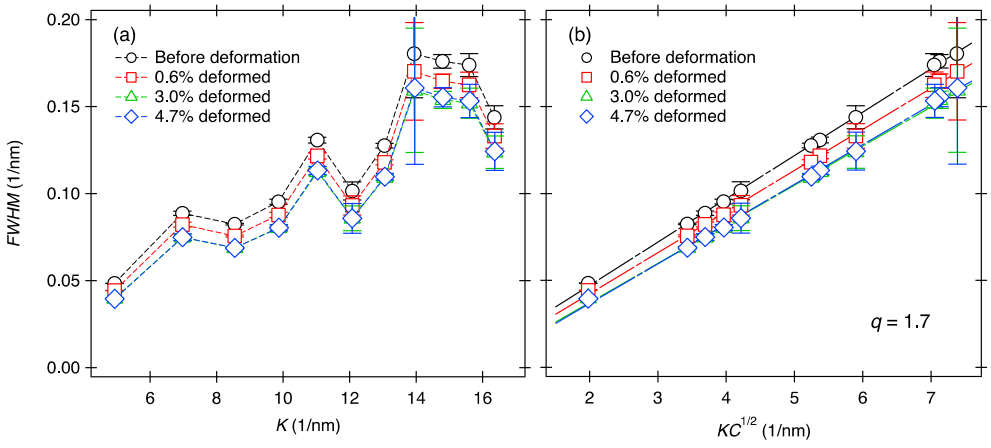

Figure 6 (a) The *FWHM* values of the physical profiles free from instrumental effects as provided by the CMWP procedure versus K=1/d for the martensite steel before deformation and at the 0.6%, 3% and 4.7% tensile deformed states. (b) The same *FWHM* values as in (a) versus $K\sqrt{\bar{C}}$ in the modified W-H plot with q = 1.7. (color for online only)

The slopes of the straight lines in Figure 6(b) decreased slightly with increasing macroscopic strain. Note that the profile does have widths and tails. The tails are, however, ignored in the *FWHM* values. We found that the decrease in the *FWHM* was also accompanied by changing in the peak shape from the Gaussian to Lorentzian type. This peak shape change is speculated to be associated with the change in the dislocation arrangement. The dislocation densities, characters and arrangements as the results by the whole profile analyses using the CMWP procedure will be discussed in details in the next sections.

3.3 Dislocation characteristics from CMWP analysis assuming symmetrical peak profile

In this report, first, we explain the results of the CMWP analysis with an assumption that the symmetrical peak profile was kept during whole tensile deformation, though we have reported that the symmetrical diffraction peak profiles before tensile deformation turned to be characteristically asymmetric due to plastically straining [17]. This analysis was performed to get average dislocation densities, and compare the obtained results with the dislocation densities measured by STEM observations and determined by the CMWP analysis considering peak asymmetry described later.

Figure 7 shows the observed and CMWP-fitted neutron diffraction patterns before tensile deformation. In the CMWP fitting, the second phase of γ was also analyzed to exclude its influence on the results of the main phase of martensite. The parameters obtained by the CMWP fitting for the axial direction are summarized in Figure 8. The parameters are labeled as the average here to express results from all packets regardless of the presence of SO and HO. The value of the average ρ (ρ_{ave}) before tensile deformation was already very high at approximately 4.0×10^{15} m^{-2}. This value is consistent with that reported in a lath martensite steel with a similar carbon content (0.18 mass%) studied using TEM [35]. This high value is created by martensitic transformation, which is difficult to be achieved by plastic tensile deformations. The value of ρ_{ave} changed a little with increasing macroscopic strain, although an increase in the flow stress was observed. The area weighted crystallite size $\langle x \rangle_{area}$ was approximately 60 nm, which is in the order of the lath size. The $\langle x \rangle_{area}$ value was almost unchanged during tensile deformation.

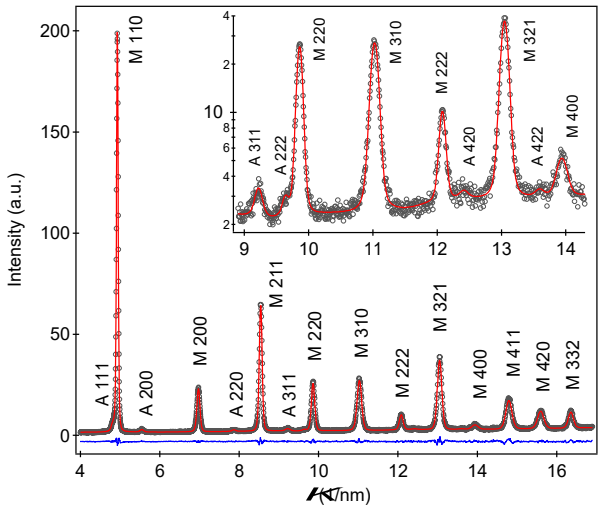

Figure 7 The observed (black-circle symbol) and CMWP fitted (red line) neutron diffraction profiles before tensile deformation. $K = 1 / d$, where d is the lattice spacing. Blue line is the residual between the fitted and the observed profiles. The up-right figure is the enlarged profiles with log scale in the vertical axis for the K values of 8.9 to 14.3 (1/nm). M or A indicates martensite or retained austenite, respectively. (color for online only)

A parameter M, which is a product of the effective cut-off radius of dislocation Re and the square root of ρ ($M = Re\sqrt{\rho}$) [20], displays the dislocation arrangement. A small or large value of M represents that the dipole character and the screening of the displacement field of dislocations are strong or weak, respectively. As shown in Figure 8, the value of average M (M_{ave}) at the as-quenched state was high. The value of M_{ave} decreased rapidly at the beginning of plastic tensile deformation, and then gradually varied with the progress of tensile deformation, finally becoming approximately 1.0. This indicates that randomly distributed dislocations at the as-quenched state rearrange towards a dipole character or a highly correlated arrangement caused by tensile deformation. These ρ_{ave} and M_{ave} values laid on the same experimental curves for the results obtained in cold-rolled lath martensite steel plates when they were replotted as a function of the equivalent plastic strain. Similar tendencies for ρ_{ave} and M_{ave} with respect to the reduction of thickness were also observed by means of XRD in a carbon-free Fe–18Ni alloy after cold rolling [36]. These results suggest that the interaction between dislocations and solute carbon atoms do not affect such

re-arrangement of dislocations during RT deformation.

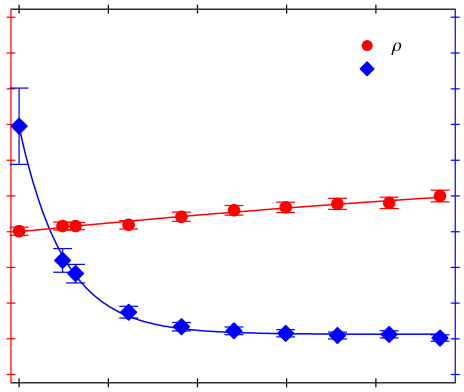

Figure 8 Dislocation densities and values of parameter *M* obtained from the CMWP fitting assuming symmetrical peak profile for the axial direction. (color for online only)

TEM observations were performed to confirm such a change in dislocation density more clearly, though the CMWP fitting for TOF neutron diffraction profiles have already been demonstrated to show a good reliability [37]. Figure 9(a) shows STEM-BF and STEM-ADF images obtained from the specimen before tensile deformation, and Figure 9(b) shows the images after 4.7% tensile deformation. The dislocation densities were determined using three ADF images with the incident beam parallel to <111> and two images for <001> (all $a/3$ <111>-type dislocations were visible under these incident beam conditions). The ρ_{ave} value before tensile deformation was determined to be between 8.79×10^{14} and 1.48×10^{15} m^{-2} (average: 1.17×10^{15} m^{-2}), which was quite close to the value by TEM work reported by Morito et al. [35] for a lath martensite steel with a similar carbon concentration (average: 1.11×10^{15} m^{-2} in an Fe–0.18C steel). Meanwhile, the ρ_{ave} value after 4.7% tensile deformation was determined to be between 9.05×10^{14} and 1.45×10^{15} m^{-2} (average: 1.18×10^{15} m^{-2}), showing no significant difference between the two conditions. These values are lower than those determined by the CMWP method using the ND profiles presented in Figure 8. The dislocation densities determined by TEM are lower than those by diffraction methods in many cases. This is because, in lath martensite case, the present TEM observations counted mainly dislocations located inside of lathes whereas the CMWP method evaluated all dislocations including those at the sub-boundaries. Huang et al. [38] have reported that

the total dislocation density in lath martensite of an interstitial free steel containing Mn and B is the sum of dislocations in sub-block boundaries (2×10^{14} m^{-2}) and those in lath boundaries (3×10^{14} m^{-2}) (they are called dislocation boundaries in [38]), and dislocations in the volume between boundaries (3×10^{14} m^{-2}). They evaluated dislocation boundaries using the misorientation angle of sub-block or lath boundary and the boundary area per unit area of sub-block or lath. Because the present steel contains 0.22 mass% carbon, the dislocation boundaries must be higher than those reported by Huang et al. [38]. Hence, it would be roughly estimated that the total dislocation density is three times higher than that inside of lath. In conclusion, the results confirm that the change in the ρ_{ave} value during tensile deformation is small, but does not exhibit a decreasing trend. The decreasing of ρ value with the progress of deformation determined using the classical W-H plot based on the peak width reported in [4, 5] must not be acceptable, because the whole peak shape including the tail part was not taken into the analysis.

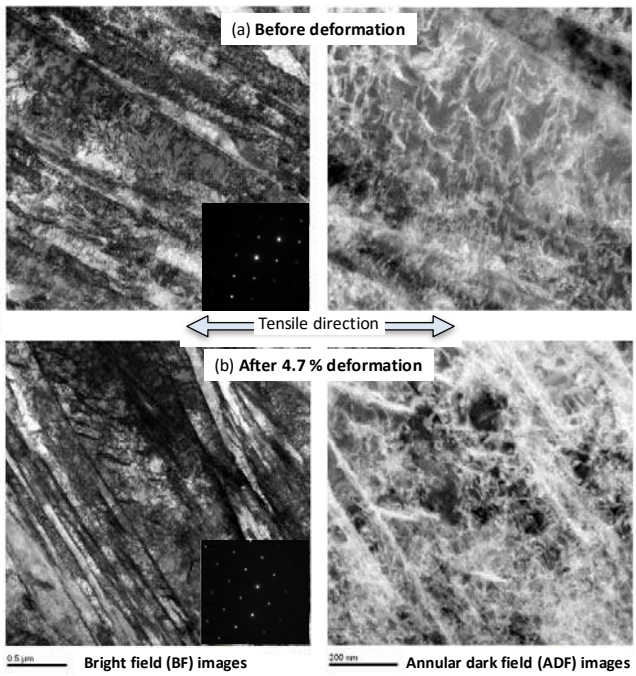

Figure 9 STEM images (a) before tensile deformation and (b) after tensile deformation to 4.7 %. The incident beam was parallel to <001> orientation.

3.4 Characteristics of dislocations obtained by the CMWP analysis with dual-packet

contribution

As described in our previous paper [17], the diffraction patterns of plastically strained martensite steel revealed characteristically asymmetric peak profiles. We have proposed a fitting procedure to analyze the ND patterns at unloaded states after plastic tensile deformations using a dual-packet contribution composing of two BCC structures, both in the Rietveld and the CMWP analyses. These analyses were not able to be performed for the ND patterns taken during loading, because statistical accuracy of the data was insufficient. The fraction of HO (f_{HO}) was found to be approximately 50% and was unchanged during tensile deformation. This was supported by a crystallographic relationship in low carbon martensite, *i.e.,* the prior austenite (111) plane is parallel to the martensite (110) plane and the habit plane of lath martensite is nearly (110) [2,3]. For example, the orientation difference of diffracted (110) plane with respect to the lath boundary (another (110)) is either 60° or 90°, and similarly diffracted (200) plane, 45° or 90°.

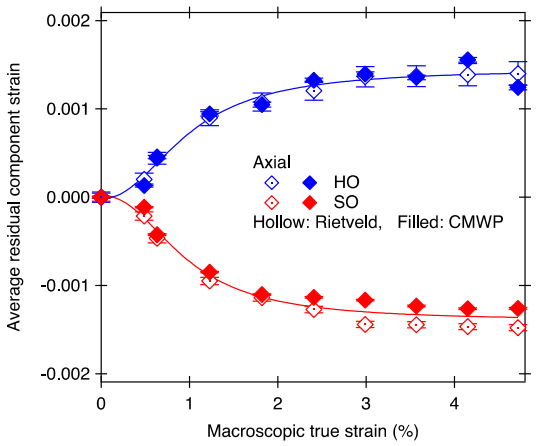

Figure 10 Residual component strain as a function of macroscopic strain in the HO and the SO analyzed using the Rietveld and the CMWP methods. (color for online only)

Next, residual strains operating in the two components of lath martensite, SO and HO, were computed using a composite model. Figure 10 shows the residual component strains in the SO and the HO measured at unloaded states after plastic tensile deformations for the axial direction. The results obtained from both the Rietveld and CMWP analyses were in good agreement within analytical errors. The residual component strains in the SO were compressive while those in the HO were tensile, and

their absolute values became larger with increasing macroscopic strain. This indicates that work softening occurs in the SO whereas work hardening in the HO. The increases in the values of residual component strains in the SO and HO became small above a macroscopic strain value of about 2.5%, where the increase in the flow stress in Figure 1 was also small. The difference in the residual component strain at the largest macroscopic true strain was about 0.29% (approximately 570 MPa).

Figure 11 shows lattice strain partitioning behavior among γ, SO and HO. The lattice strain responses to the applied stress in Figure 4(a) were smooth-interpolated, and the residual component stresses were considered to be balanced at the martensite phase stresses for the related applied stresses, by assuming that the Young moduli of SO and HO were identical and that there were no stress-relaxation during unloading. The lattice strain of γ showed the largest value during macroscopic plastic tensile deformation, however its contribution to the whole flow stress was less than 6% because of its small volume fraction. Therefore, the HO is considered to play the most important role in the work-hardening in this specimen during tensile deformation.

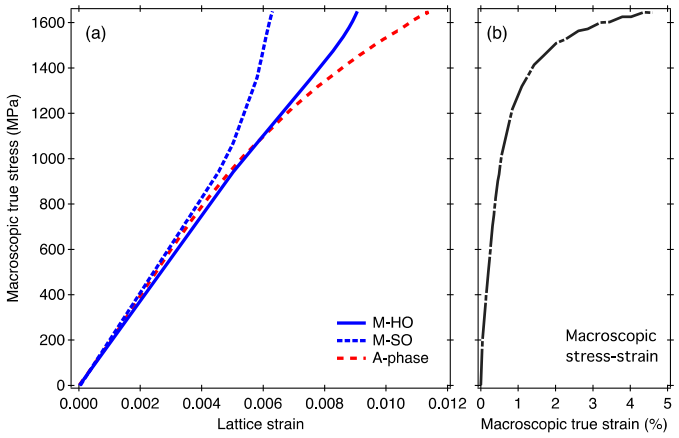

Figure 11 (a) Lattice strain partitioning during tensile deformation estimated from the lattice strains in Figure 4(a) and the residual component strains in Figure 10. M or A indicates martensite or retained austenite, respectively. (b) The relevant macroscopic stress-strain data. (color for online only)

Figure 12(a) shows the dislocation densities in packet components (ρ_{HO} for HO and ρ_{SO} for SO) obtained from the CMWP fitting assuming the dual-packet contribution. The ρ_{HO} value increased with increasing macroscopic strain to be in the order of 10^{16}

m^{-2}, while the ρ_{SO} value decreased rapidly at the beginning of deformation to be in the order of 10^{14} m^{-2}, and then hardly changed during deformation. Further details of the ρ_{HO} and the ρ_{SO} have been reported in our previous paper [17]. The total average dislocation density (ρ_t) that was calculated from the ρ_{HO} and ρ_{SO} values as the weighted average, according $\rho_t = f_{HO}\,\rho_{HO} + (1 - f_{HO})\,\rho_{SO}$, showed similar tendency with the ρ_{ave} value shown in Figure 8, but with slightly larger values. It is important to note here that the ρ_{ave} values in Figure 8 were obtained by the CMWP procedure assuming the symmetrical profile, whereas the ρ_{HO} and ρ_{SO} were provided with allowing the existence of two different packet populations. By this procedure the asymmetries in the peak profiles were correctly taken into account, and the obtained results are considered the physically correct ones.

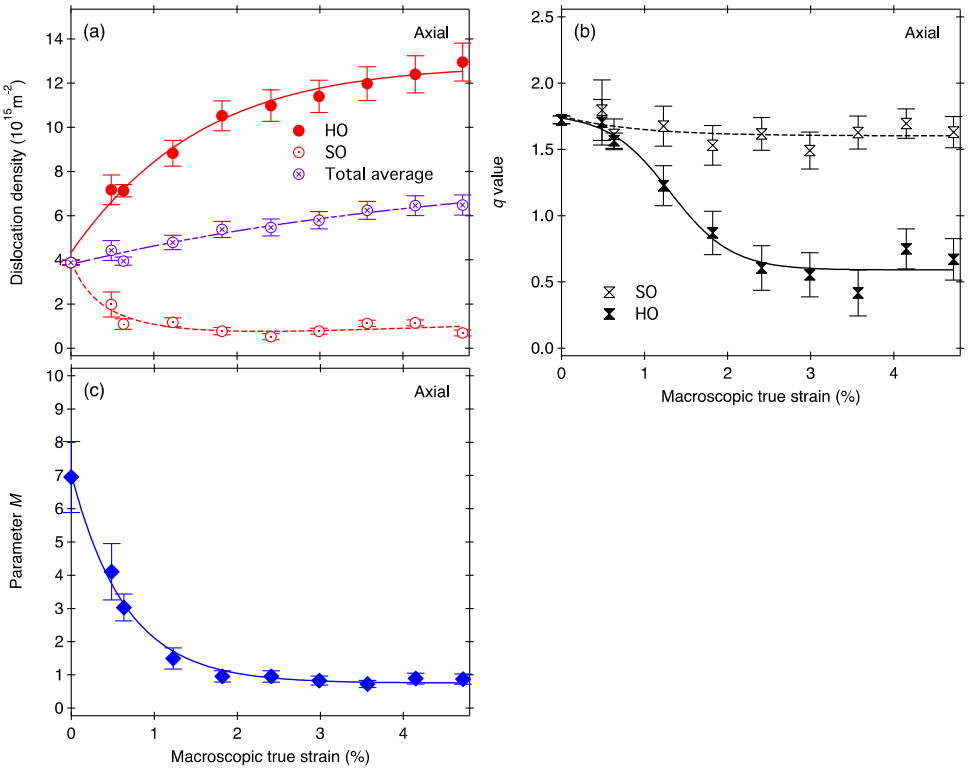

Figure12 (a) Dislocation density in packet component for the HO or SO, (b) parameter depending on the dislocation character (q) for the HO or SO, and (c) arrangement parameter M in the HO, obtained from the CMWP fitting assuming multi-packet contribution for the axial direction. (color for online only)

Figure 12(b) shows the q values for the HO and SO (q_{HO} and q_{SO}). The q value obtained before tensile deformation was approximately 1.7, indicating that before tensile deformation the dislocations have a mixed character of edge and screw with a larger proportion of screw-type. Screw-type dislocations are mainly found in BCC polycrystalline materials [33,39]. The q_{SO} values were almost unchanged with deformation from the state before tensile deformation, indicating that dislocations with a screw character are dominant in the SO. In the contrary, the q_{HO} value decreased largely at the beginning of tensile deformation to be about 0.6, indicating that the proportion of edge dislocations increased in the HO. These results support the simulation of our previous paper (Table 1 in [17]). Screw dislocations can move in any direction, and therefore annihilate relatively easily even when they are far apart from each other [40]. Edge dislocations have to climb for annihilating, and therefore can annihilate only within short distances [40].

The q value of 1.7 that hardly changed and the dislocation density that decreased during deformation in the SO, are consistent with the results of the modified W-H plot, as described in section 3.2, where good linearity was kept using q = 1.7 and where the slopes decreased slightly with increasing macroscopic strain. Therefore, it can be understood that the *FWHM* values of the profiles are mainly of the profile-parts of the SO. It was shown in our previous paper (Figures 5(c) and 5(d) in [17]) that the total physical diffraction profiles in the plastically tensile deformed martensite consisted of two peaks. The ones with larger intensity and smaller *FWHM* corresponded to the SO, whereas the other ones with smaller intensity but larger *FWHM* corresponded to the HO. The *FWHM* values, shown in Figure 6, obviously correspond to the larger intensity peaks where the *FWHM* values decrease slightly with strain.

Figure 12(c) shows the values of parameter M for HO (M_{HO}). The M_{HO} value was high at the as-quenched state. It decreased rapidly at the beginning of deformation, and then gradually lowered with the progress of tensile deformation, finally becoming less than 1.0. This behavior is very similar to that of M_{ave} shown in Figure 8. Meanwhile, the values of the parameter M for SO (M_{SO}) were kept at high values during tensile deformation. The high value of M_{SO} suggests that it has little effect on the dislocation densities, due to the balanced competition of dislocation generation and annihilation resulting in small work softening.

4. Discussion

4.1 The α coefficient in Taylor's equation

Since the average dislocation densities in the present lath martensite steel were found hardly to change during plastic tensile deformation, the observed large work hardening is predicted to have a relation with an increase in the α coefficient of Taylor's equation. The α coefficients for HO (α_{HO}) and for SO (α_{SO}) for this specimen can be estimated from the macroscopic stress−strain curve and the values of ρ_{HO} and ρ_{SO} based on a composite model using the following equation:

$$\Delta\sigma = \sigma - \sigma_0 = \alpha\, \mu\, M_T\, b\, (f_{HO}\, \alpha_{HO} \sqrt{\rho_{HO}} + (1 - f_{HO})\, \alpha_{SO} \sqrt{\rho_{SO}}) . \quad (7)$$

Here the values of σ_0, μ, M_T, and b used in the calculations were 350 MPa, 77.3 GPa, 2.8, and 0.248 nm, respectively. The α_{SO} value was determined at the beginning of deformation to be about 0.18, and was fixed during further tensile deformation because of the work softening in the SO.

Figure 13 shows the calculated α_{HO} values. It is obvious that the α_{HO} value increases rapidly at the beginning of plastic deformation, and then gradually varies with the progress of tensile deformation. The α_{HO} value saturates at about 0.4, which is known as the value frequently used for metallic materials [41]. The α coefficient has been, however, regarded to be constant during deformation in many studies [42–44], but the values varied widely in other literatures [42,43]. It is known that the α coefficient is determined from the angle between adjacent dislocation segments at a point where the dislocation breaks free from an obstacle [45].

From the *in situ* neutron diffraction study during tensile loading for a stainless steel, the α coefficients was found to be different depending on individual <*hkl*> grain families. It was large in <*hkl*> grain families with larger Schmid factors in which dislocations were arranged in longitudinal bands frequently divided by sub-boundaries, but low in the others with smaller Schmid factors in which cell structure was evolved [37].

4.2 Parameter M and work hardening relationship

The dislocations in as-quenched lath martensites are randomly arranged, as is interpreted from the value of *M* before tensile deformation obtained in this study. This feature has been observed with TEM in previous reports [4,38,46]. The dislocation arrangement changed and the lath boundaries became difficult to be distinguished when

the lath martensite steels were cold–rolled. Nakashima et al. [4] observed that the lath boundaries changed to cell structures with dense dislocation walls after 10% cold rolling, while Hughes and Hansen [47] also observed the appearance of a shear band after 30% cold rolling. The decrease of parameter M measured in this study can therefore be explained by such transitions of dislocation arrangements with plastic tensile deformation.

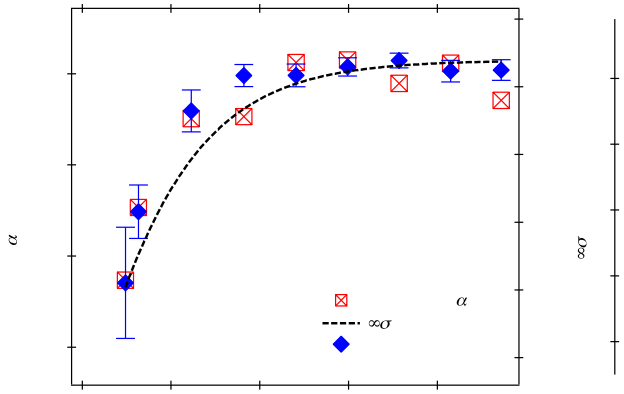

Figure13 The coefficient α values calculated from the dislocation densities according to the Taylor's equation shown in Eq. (7), and their relations with the change of flow stress due to dislocations and the parameter M determined from the stress-strain curve, for the HO. (color for online only)

The $\Delta\sigma$ values and values of parameter M_{HO} are superimposed in Figure 13. Note that the vertical axis for M_{HO} value in Figure 13 is in a reverse order. As a result, a rapid increase in the $\Delta\sigma$ value is proportional to a rapid decrease in parameter M_{HO}, which relates to an increase in the α_{HO} coefficient. The changing of the α coefficient while the dislocation arrangement is changing during plastic tensile deformation, has recently been discussed in detail by Mughrabi [48]. Schafler et al. [49] have also claimed that parameter M can be linked to the α coefficient in the Taylor equation of flow stress, though their results were not in a direct relation.

It can be concluded according to the above results and discussion that the decrease of parameter M in the as-quenched martensite during tensile deformation is related to the variation of the dislocation arrangement, and that these are speculated to change the stress field for dislocation mobilization appearing as an increase in the α coefficient of

the Taylor's equation.

5. Conclusions

In situ neutron diffraction was performed during tensile deformation of an as-quenched lath martensite steel containing 0.22 mass% of carbon, which showed an extremely large work hardening at the beginning of plastic deformation, using a high-resolution TOF neutron diffractometer.

(1) The dislocation density of an as-quenched lath martensite was in the order of 10^{15} m^{-2}. The average dislocation density obtained from the CMWP method revealed little change during tensile deformation, which was in good agreement with the results obtained by microstructure observations using STEM.

(2) The diffraction peaks at plastically deformed states were asymmetries as the reflection of partitioning of the load and different dislocation densities/arrangements in the two lath-packets where the dislocation glides are favorable (SO) and unfavorable (HO). During tensile straining, the dislocation density increased in the HO accompanying an increase in the load sharing showing work-hardening, while decreased in the SO followed with work-softening. The dislocation character and dislocation arrangement varied also in the HO, but hardly changed in the SO. In the HO, dislocations that were mainly of screw-type at the as-quenched state varied to be mainly of edge-type, and the random arrangement at the as-quenched state rearranged towards a dipole character or a highly correlated arrangement.

(3) The HO played an important role in the work hardening in the lath martensite steel during tensile deformation.

(4) The extremely large work hardening could not be described sufficiently only by the increase of dislocation density but also the change of dislocation arrangement. The α coefficient of the Taylor's equation should be considered by taking into account the dislocation arrangement, which could be postulated from the variation in the parameter M determined by the CMWP method.

ACKNOWLEDGMENTS

The authors acknowledge Prof. Shigeo Sato of Ibaraki University for the valuable discussion. The neutron diffraction experiments were performed at BL19 in Materials and Life Science Facility of J-PARC with the proposals of 2014I0019 and 2014P0102,

and got partly financial supports from the Japan Society for the Promotion of Science Grant-in-Aid for Scientific Research (grant numbers 26289264, 15H05767) and Education Commission of Hubei Province of China (grant number B20161203).

REFERENCES

1. T. Maki: *Proc. 1st Int. Symp. on Steel Sci.*, 2007, pp. 1–10.
2. S. Morito, H. Tanaka, R. Konishi, T. Furuhara and T. Maki: *Acta Mater.*, 2003, vol. 51, pp. 1789–99.
3. H. Kitahara, R. Ueji, N. Tsuji and Y. Minamino: *Acta Mater.*, 2006, vol. 54, pp. 1279–88.
4. K. Nakashima, Y. Fujimura, H. Matsubayashi, T. Tsuchiyama and S. Takaki: *Tetsu-to-Hagane*, 2007, vol. 93, pp. 459–65.
5. S. Morooka, Y. Tomota and T. Kamiyama: *ISIJ Int.*, 2008, vol. 48, pp. 525–30.
6. G.K. Williamson and R.E. Smallman: *Phil. Mag.*, 1956, vol. 1, pp. 34–46.
7. G.I. Taylor: *Proc. R. Soc. A*, 1934, vol. 45, pp. 362–87.
8. T. Ungár, L. Li, G. Tichy, W. Pantleon, H. Choo and P.K. Liaw: *Scripta Mater.*, 2011, vol. 64, pp. 876–79.
9. B. Hutchinson, D. Lindell and M. Barnett: *ISIJ Int.*, 2015, vol. 55, pp. 1114–22.
10. M.R. Daymond, C.N. Tomé and M.A.M. Bourke: *Acta Mater.*, 2000, vol. 48, pp. 553–64.
11. Y. Tomota, P. Lukas, S. Harjo, J-H. Park, N. Tsuchida and D. Neov: *Acta Mater.*, 2003, vol. 51, pp. 819–30.
12. Y. Tomota, H. Tokuda, Y. Adachi, M. Wakita, N. Minakawa, A. Moriai and Y. Morii: *Acta Mater.*, 2004, vol. 52, pp. 5737–45.
13. M.R. Daymond, C. Hartig and H. Mecking: *Acta Mater.*, 2005, vol. 53, pp. 2805–13.
14. O. Muransky, P. Sittner, J. Zrnik and E.C. Oliver: *Acta Mater.*, 2008, vol. 56, pp. 3367–79.
15. S. Harjo, J. Abe, K. Aizawa, W. Gong and T. Iwahashi: *JPS Conf. Proc.*, 2014, vol. 1, 014017 (6 pages).
16. S. Morooka, T. Tsuchiyama, S. Harjo and K. Aizawa: *CAMP-ISIJ*, 2014, vol. 168, p. 866.

17. T. Ungár, S. Harjo, T. Kawasaki, Y. Tomota, G. Ribarik and Z. Shi: *Metall. Mat. Trans. A*, 2016, online available.
18. H. Mughrabi, T. Ungár, W. Kienle and M. Wilkens: *Philos. Mag. A*, 1986, vol. 53, pp. 793–813.
19. B. Jakobsen, H.F. Poulsen, U. Lienert, J. Almer, S.D. Shastri, H.O. Sørensen, C. Gundlach and W. Pantleon: *Science*, 2006, vol. 312, pp. 889–92.
20. T. Ungár, J. Gubicza, G. Ribarik and A. Borbely: *J. Appl. Cryst.*, 2001, vol. 34, pp. 298–310.
21. G. Ribarik and T. Ungár: *Mater. Sci. Eng. A*, 2010, vol. 528, pp. 112-21.
22. Z. Shi, K. Liu, M. Wang, J. Shi, H. Dong, J. Pu, B. Chi, Y. Zhang and L. Jian: *Met. Mater. Int.*, 2012, vol. 18, pp. 317–20.
23. S. Harjo, T. Ito, K. Aizawa, H. Arima, J. Abe, A. Moriai, T. Iwahashi and T. Kamiyama: *Mater. Sci. Forum*, 2011, vol. 681, pp. 443–48.
24. R. Oishi, M. Yonemura, Y. Nishimaki, S. Torii, A. Hoshikawa, T. Ishigaki, T. Morishima, K. Mori and T. Kamiyama: *Nucl. Instrum. Meth. A*, 2009, vol. 600, pp. 94–96.
25. K. Iakoubovskii, K. Mitsuishi and K. Furuya: *Nanotechnology*, 2008, vol. 19, 155705 (5 pages).
26. O.D. Sherby, J. Wadsworth, D.R. Lesuer and C.K. Syn: *Mater. Trans.*, 2008, vol. 49, pp. 2016–27.
27. Y. Tomota, H. Tokuda, S. Torii and T. Kamiyama: *Mater. Sci. Eng. A*, 2006, vol. 434, pp. 82-87.
28. L.D. Landau and E.M. Lifshitz: *Theory of Elasticity*, 1st English ed., Pergamon Press, London, 1959, pp. 1-42.
29. T.H. Courtney, *Mechanical Behavior of Materials*, 2nd ed., Waveland Press Inc., Long Grove, 1990, pp. 44-84.
30. S.A. Kim and W.L. Johnson: *Mater. Sci. Eng. A*, 2007, vol. 452-453, pp. 633–39.
31. T. Ungár and A. Borbély: *Appl. Phys. Lett.*, 1996, vol. 69, pp. 3173-75.
32. T. Ungár and G. Tichy: *Phys. Stat. Sol. (a)*, 1999, vol. 171, pp. 425–34.
33. T. Ungár, I. Dragomir, Á. Révész and A. Borbély: *J. Appl. Cryst.*, 1999, vol. 32, pp. 992–1002.
34. A. Shibata, S. Morito, T. Furuhara and T. Maki: Acta Mater., 2009, vol. 57, pp. 483–92.

35. S. Morito, J. Nishikawa and T. Maki: *ISIJ Int.*, 2003, vol. 43, pp. 1475–77.
36. D. Akama, T. Tsuchiyama and S. Takaki: *ISIJ Int.*, 2016, vol. 56, pp. 1675–80.
37. T. Ungár, A.D. Stoica, G. Tichy, X.L. Wang: *Acta Mater.*, 2014, vol. 66, pp. 251–61.
38. X. Huang, S. Morito, N. Hansen and T. Maki: *Metall. Mater. Trans. A*, 2012, vol. 43A, pp. 3517–31.
39. V. Vitek: *Phil. Mag.*, 2004, vol. 84, pp. 415–28.
40. U. Essmann and H. Mughrabi: *Philos. Mag. A*, 1979, vol. 40, pp. 731–56.
41. H. Mughrabi: *Mater. Sci. Eng.*, 1987, vol. 85, pp. 15–35.
42. N. Hansen and X. Huang: *Acta Mater.*, 1998, vol. 46, pp. 1827–36.
43. T. Waitz, H.P. Karnthaler and R.Z. Valiev: in Zehetbauer, M.J., Valiev, R.Z. (Eds.), *Nanomaterials by Severe Plastic Deformation*, 2004, Wiley-VCH, New York, pp. 337–50.
44. J.A. El-Awady: *Nat. Commun.*, 2015, vol. 6, 5926 (9 pages).
45. K. Hanson and J.W. Morris Jr.: *J. Appl. Phys.*, 1975, vol. 46, pp. 983–90.
46. S. Morito, T. Ohba, A.K. Das, T. Hayashi and M. Yoshida: *ISIJ Int.*, 2013, vol. 53, pp. 2226–32.
47. D. A. Hughes and N. Hansen: *Acta Mater.*, 2000, vol. 48, pp. 2985–3004.
48. H. Mughrabi: *Curr. Opin. Solid State Mater. Sci.*, 2016, vol. 20, pp. 411–20.
49. E. Schafler, K. Simon, S. Bernstorff, P. Hanák, G. Tichy, T. Ungár and M.J. Zehetbauer: *Acta Mater.*, 2005, vol. 53, pp. 315–22.

Table 1 The *hkl* dependent Young's modulus (E_{hkl}) values.

hkl	110	200	211	220	310	222
E_{hkl}	233(1)	167(2)	233(2)	229(3)	183(3)	250(8)

FIGURE CAPTIONS:

Figure 1 Macroscopic Stress-strain curve of as-quenched lath martensite steel in this study.

Figure 2 The observed (black-plus symbol) and Rietveld fitted (pink line) neutron diffraction profiles before tensile deformation, in which *d* is the lattice spacing. Blue line is the residual between the fitted and the observed profiles. The up-left figure is the enlarged profiles with log scale in the vertical axis for the *d* values of 0.07 to 0.112 (nm). M or A indicates martensite or retained austenite, respectively. (color for online only)

Figure 3 The fractions of retained austenite measured after plastic tensile deformations (at unloaded states). (color for online only)

Figure 4 (a) Lattice strains measured during tensile deformation and (b) residual lattice strains measured at unloaded states after plastic tensile deformations in the axial direction. M or A indicates martensite or retained austenite, respectively. (color for online only)

Figure 5 The measured $1/E_{hkl}$ values versus H^2.

Figure 6 (a) The *FWHM* values of the physical profiles free from instrumental effects as provided by the CMWP procedure versus $K=1/d$ for the martensite steel before deformation and at the 0.6%, 3% and 4.7% tensile deformed states. (b) The same *FWHM* values as in (a) versus $K\sqrt{\bar{C}}$ in the modified W-H plot with $q = 1.7$. (color for online only)

Figure 7 The observed (black-circle symbol) and CMWP fitted (red line) neutron diffraction profiles before tensile deformation. $K = 1 / d$, where *d* is the lattice spacing.

Blue line is the residual between the fitted and the observed profiles. The up-right figure is the enlarged profiles with log scale in the vertical axis for the *K* values of 8.9 to 14.3 (1/nm). M or A indicates martensite or retained austenite, respectively. (color for online only)

Figure 8 Dislocation densities and values of parameter *M* obtained from the CMWP fitting assuming symmetrical peak profile for the axial direction. (color for online only)

Figure 9 STEM images (a) before tensile deformation and (b) after tensile deformation to 4.7 %. The incident beam was parallel to <001> orientation.

Figure 10 Residual component strain as a function of macroscopic strain in the HO and the SO analyzed using the Rietveld and the CMWP methods. (color for online only)

Figure 11 (a) Lattice strain partitioning during tensile deformation estimated from the lattice strains in Figure 4(a) and the residual component strains in Figure 10. M or A indicates martensite or retained austenite, respectively. (b) The relevant macroscopic stress-strain data. (color for online only)

Figure12 (a) Dislocation density in packet component for the HO or SO, (b) parameter depending on the dislocation character (q) for the HO or SO, and (c) arrangement parameter *M* in the HO, obtained from the CMWP fitting assuming multi-packet contribution for the axial direction. (color for online only)

Figure13 The coefficient α values calculated from the dislocation densities according to the Taylor's equation shown in Eq. (7), and their relations with the change of flow stress due to dislocations and the parameter *M* determined from the stress-strain curve, for the HO. (color for online only)

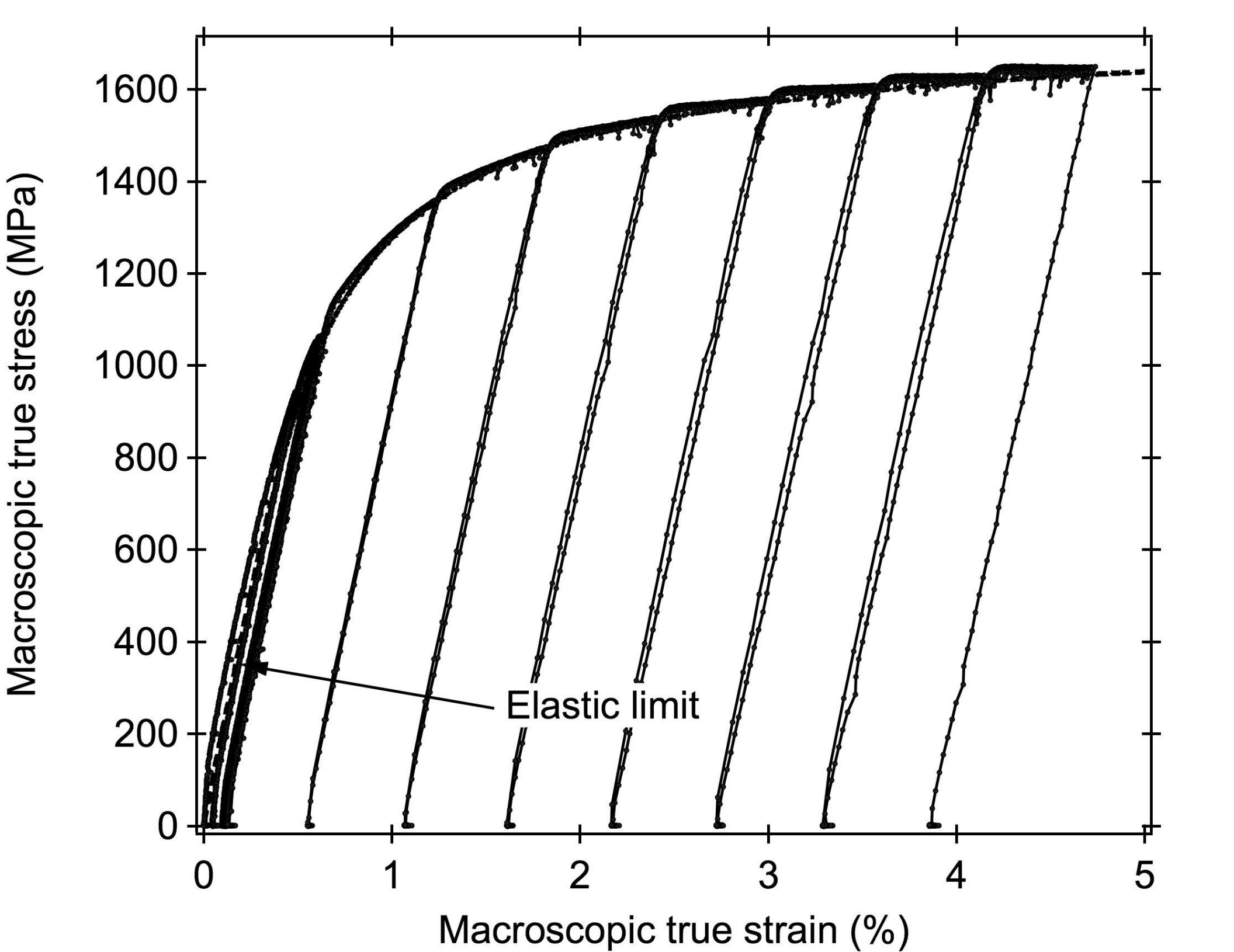
Macroscopic true stress (MPa)
1600
1400
1200
1000
800
600
400
200
0
Elastic limit
0
1
2
3
4
5
Macroscopic true strain (%)

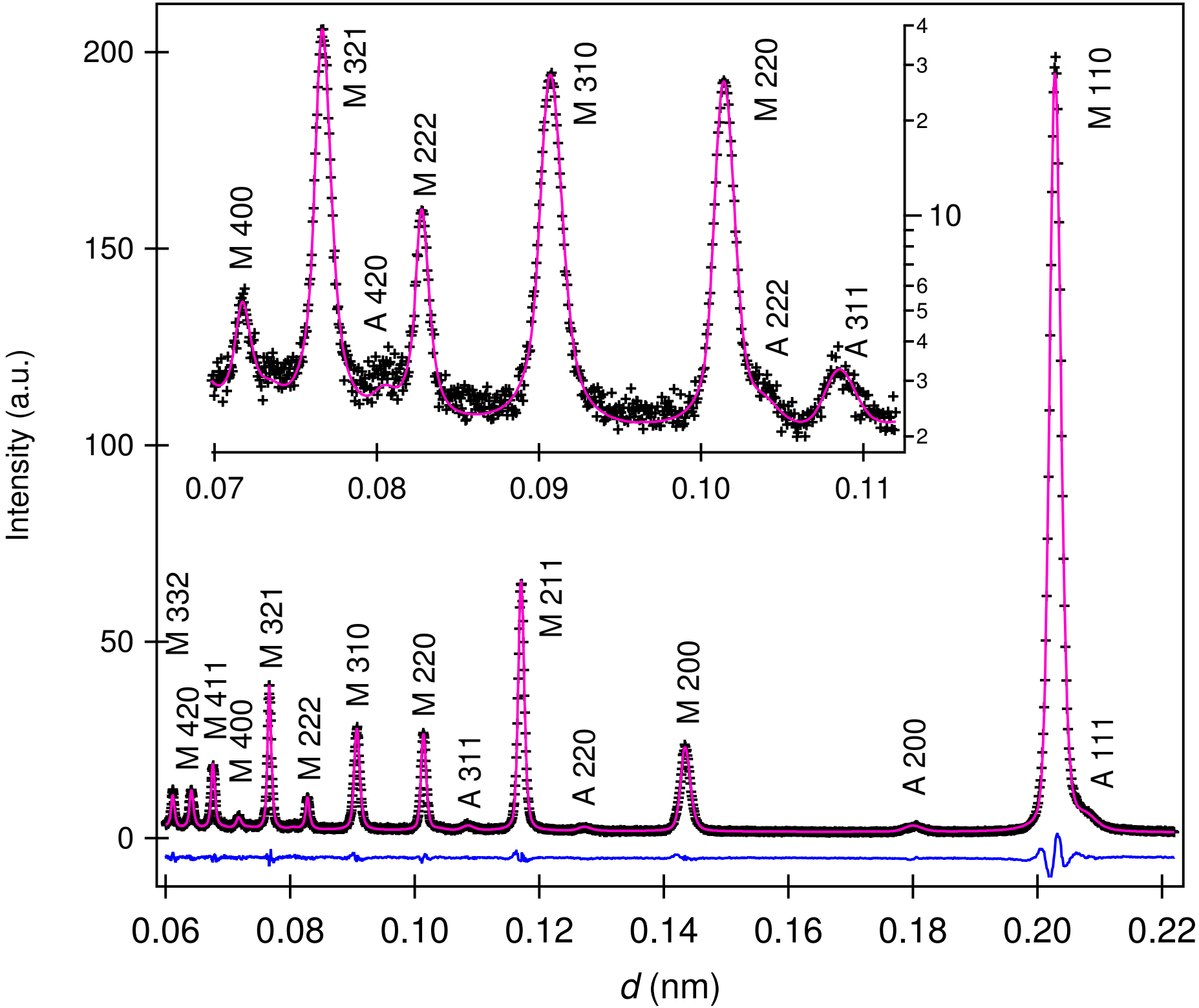
Intensity (a.u.)
d (nm)
M 332
M 420
M 411
M 400
M 321
M 222
M 310
M 220
A 311
M 211
A 220
M 200
A 200
A 111
M 110
M 400
A 420
M 222
M 321
M 310
M 220
A 222
A 311

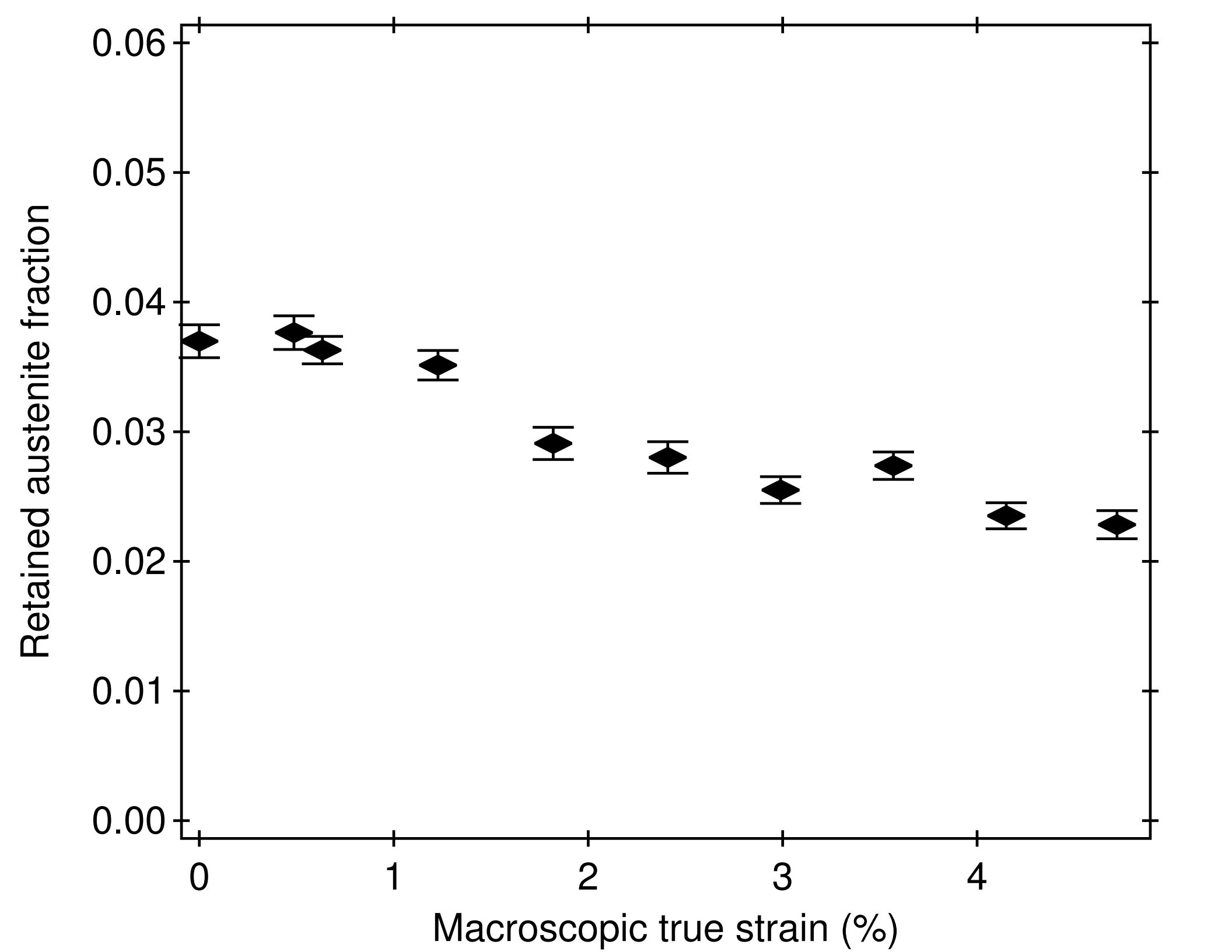
0.06
0.05
0.04
0.03
0.02
0.01
0.00
Retained austenite fraction
0
1
2
3
4
Macroscopic true strain (%)

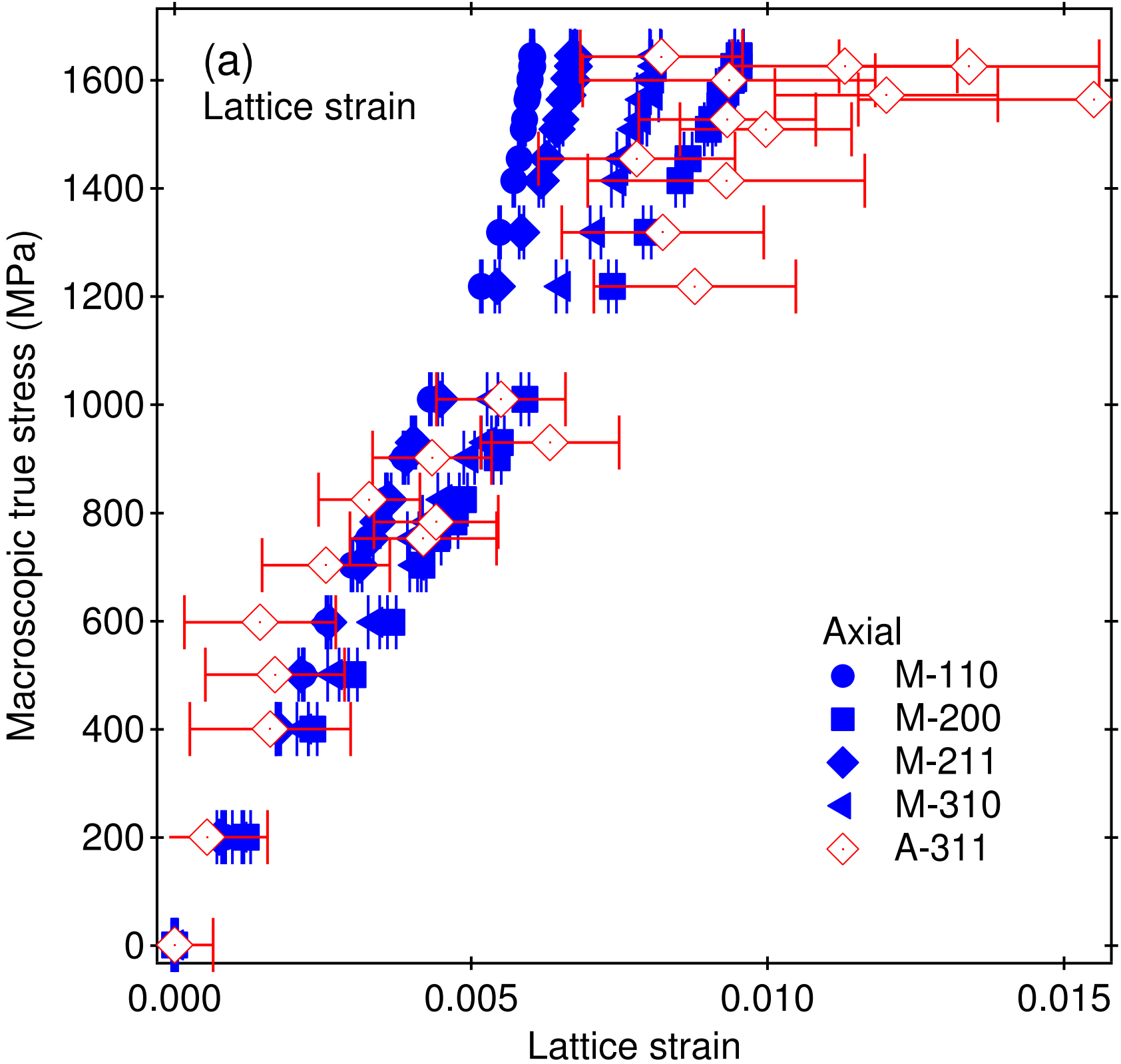
(a)
Lattice strain
Macroscopic true stress (MPa)
1600
1400
1200
1000
800
600
400
200
0
0.000
0.005
0.010
0.015
Lattice strain
Axial
M-110
M-200
M-211
M-310
A-311

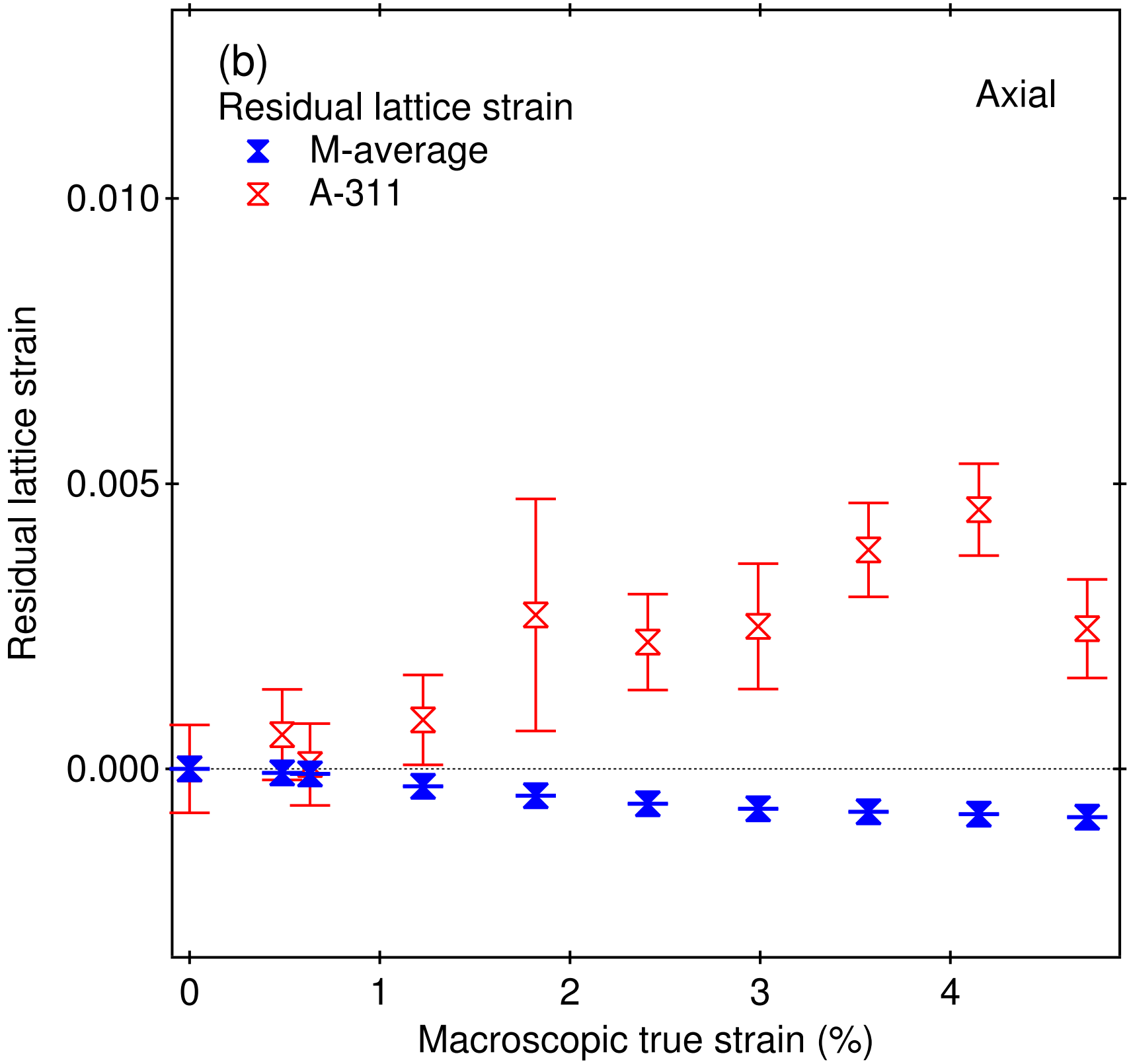
(b)
Residual lattice strain
M-average
A-311
Axial
0.010
0.005
0.000
Residual lattice strain
0
1
2
3
4
Macroscopic true strain (%)

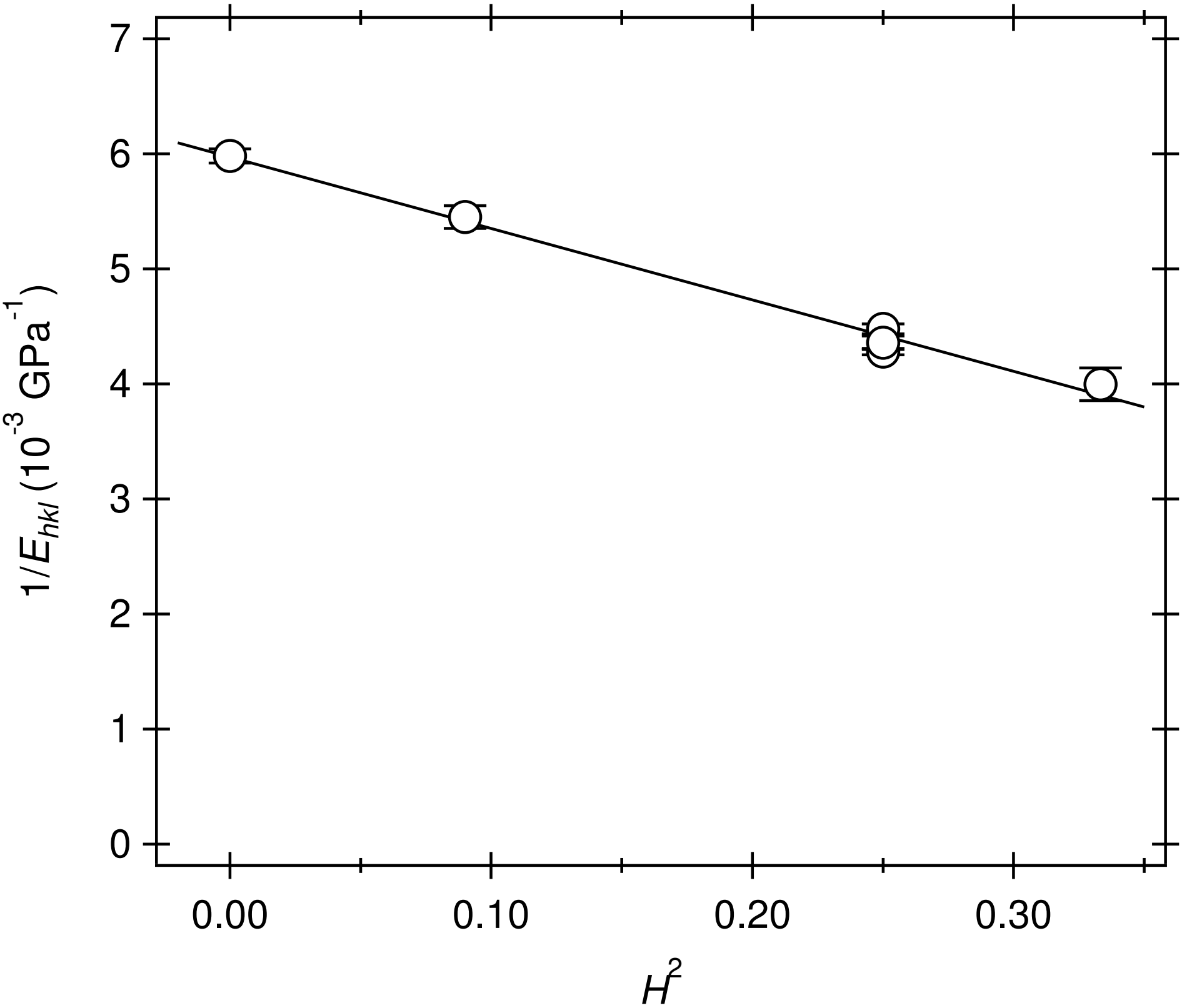
7
6
5
4
3
2
1
0
0.00
0.10
0.20
0.30
$1/E_{hkl}$ (10^{-3} GPa^{-1})
H^2

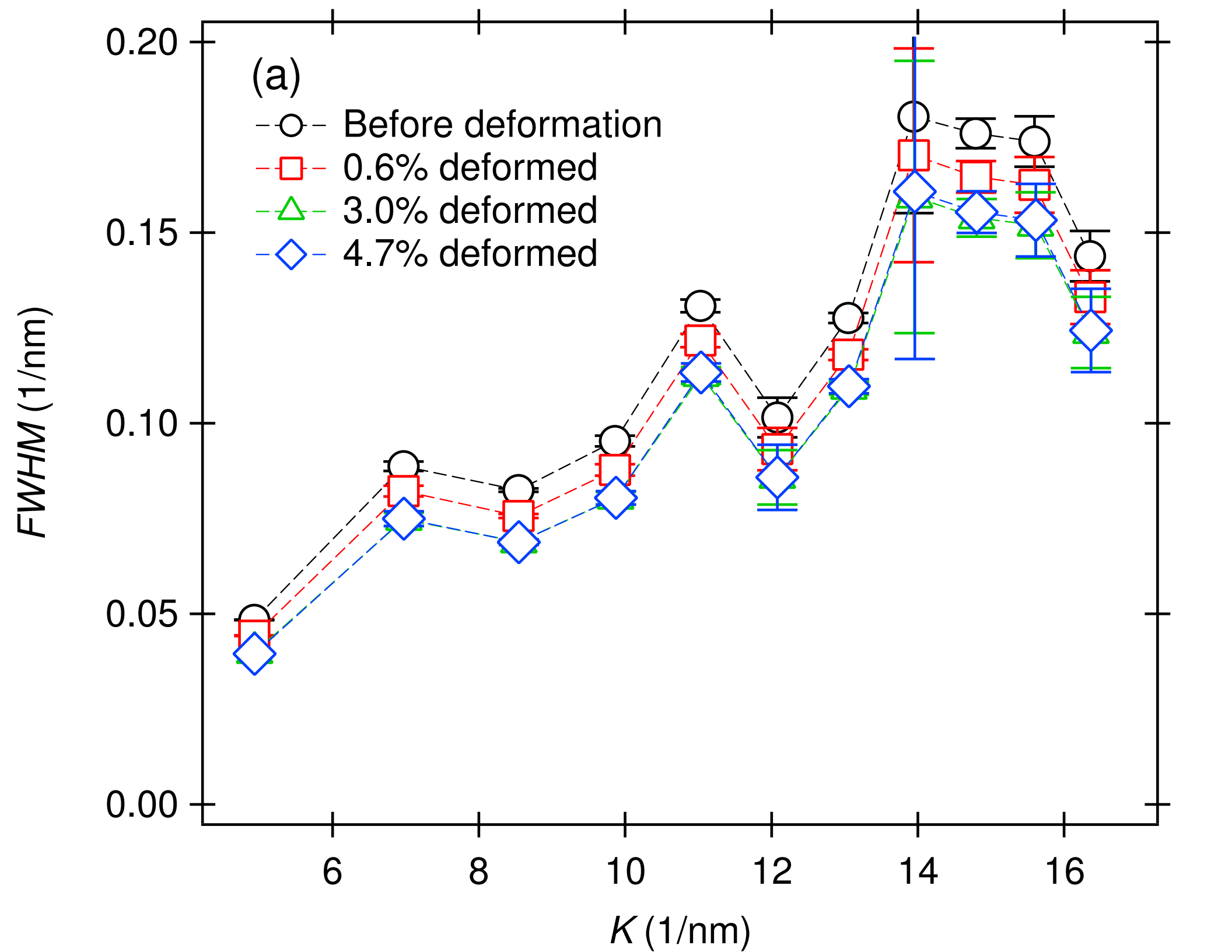
(a)
Before deformation
0.6% deformed
3.0% deformed
4.7% deformed
0.20
0.15
0.10
0.05
0.00
FWHM (1/nm)
6
8
10
12
14
16
K (1/nm)

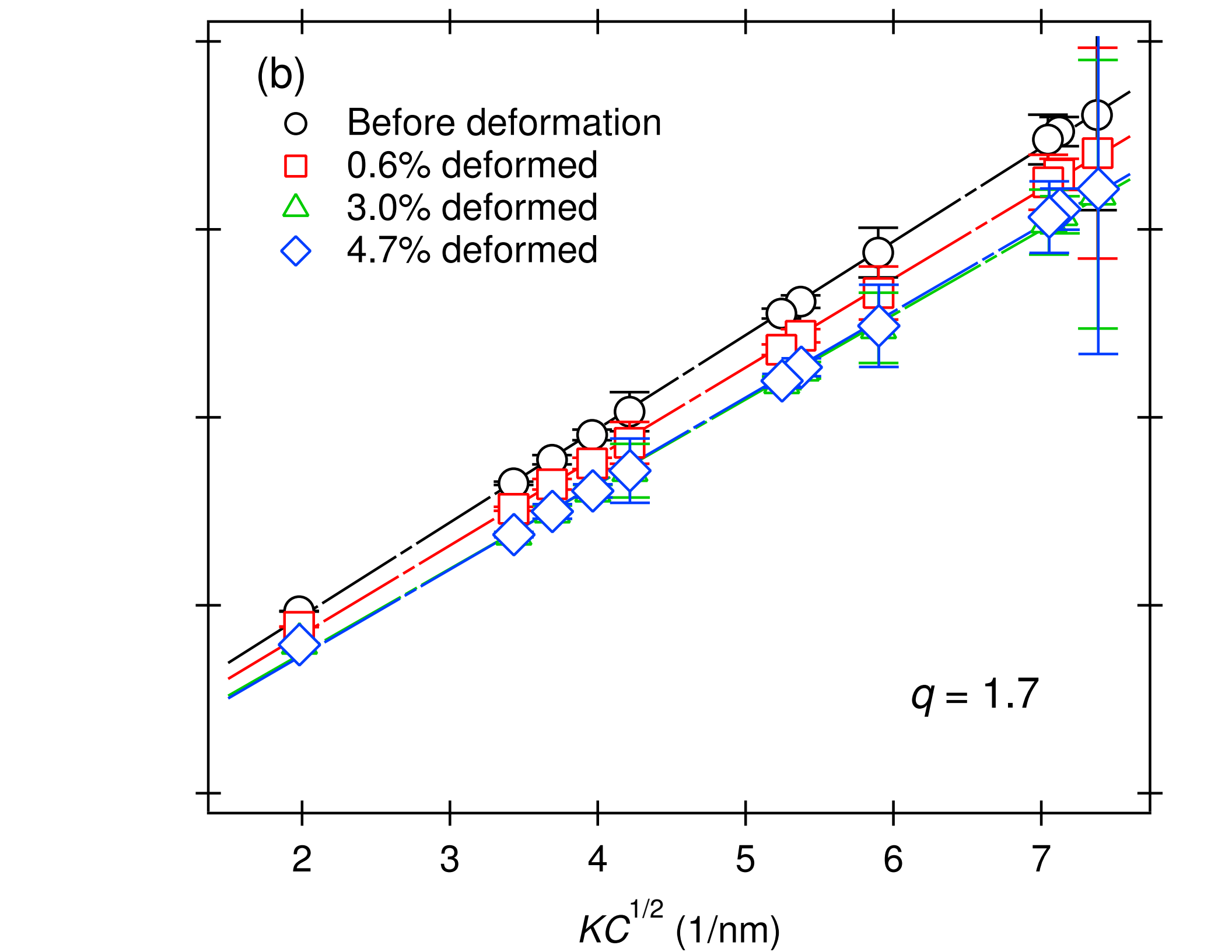
(b)
Before deformation
0.6% deformed
3.0% deformed
4.7% deformed
q = 1.7
2
3
4
5
6
7
KC^1/2 (1/nm)

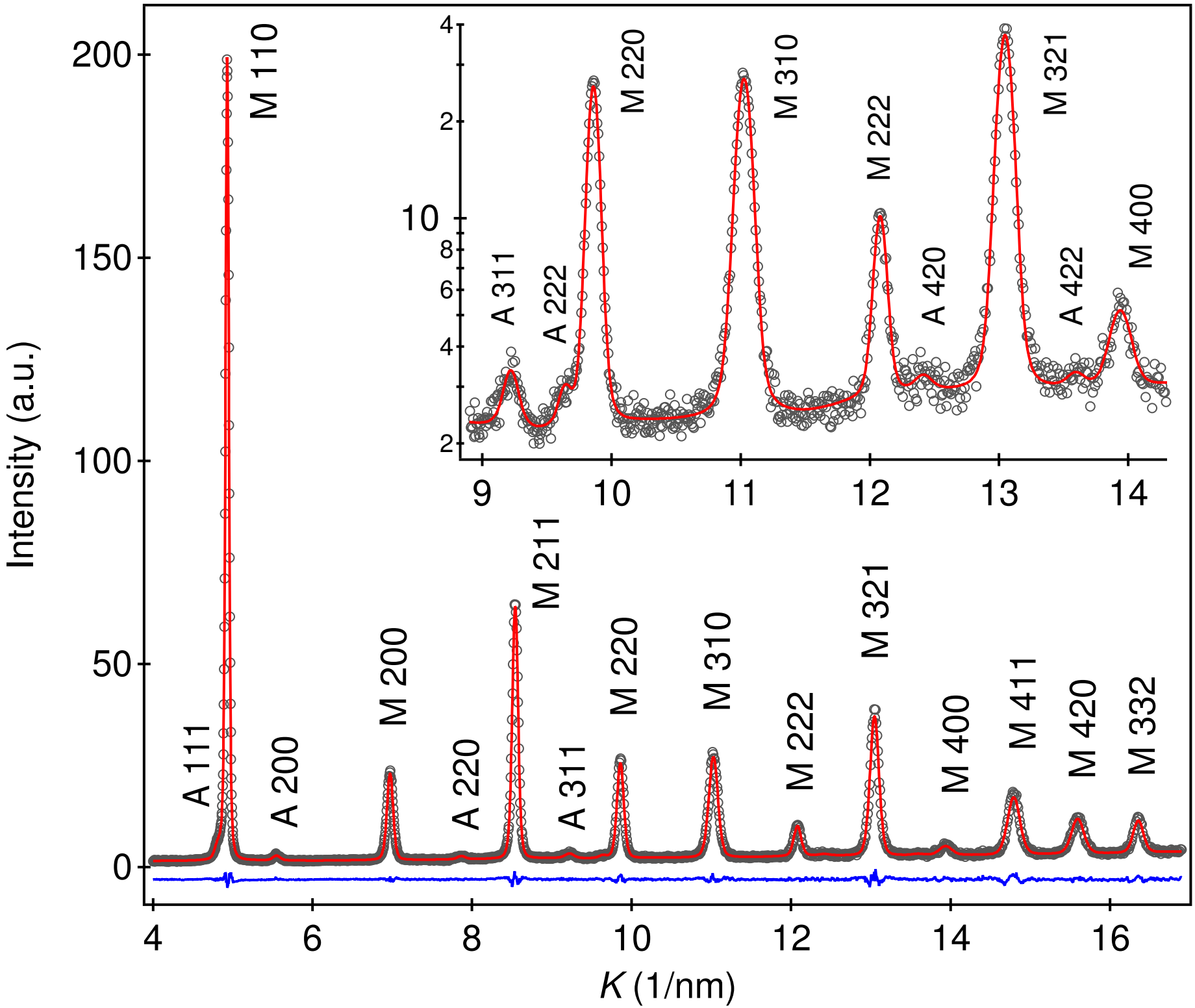
Intensity (a.u.)
K (1/nm)
A 111
A 200
M 200
A 220
M 211
A 311
M 220
M 310
M 222
M 321
M 400
M 411
M 420
M 332
M 110
A 311
A 222
M 220
M 310
M 222
A 420
M 321
A 422
M 400

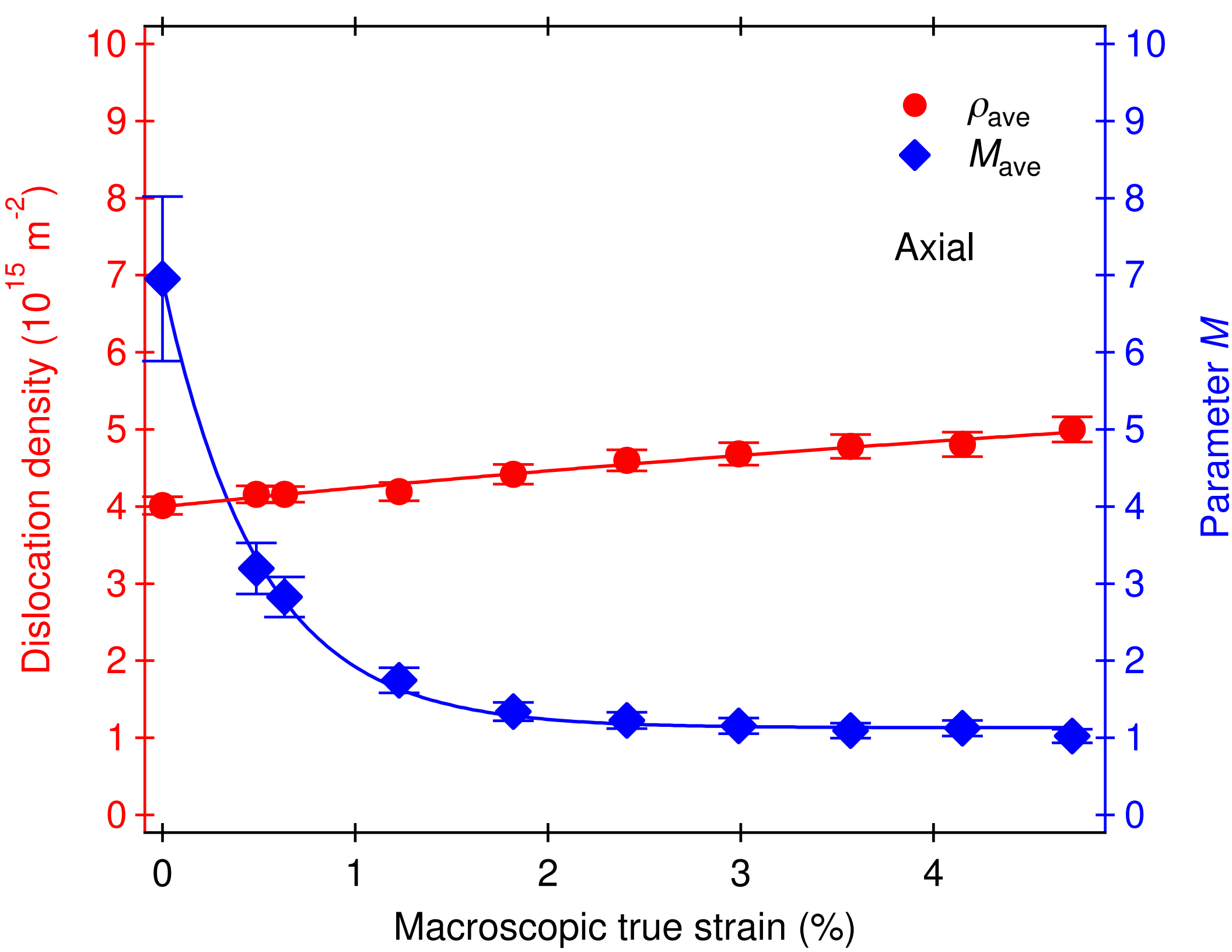
Dislocation density (10^{15} m^{-2})
Parameter M
Macroscopic true strain (%)
ρ_{ave}
M_{ave}
Axial
0
1
2
3
4
5
6
7
8
9
10

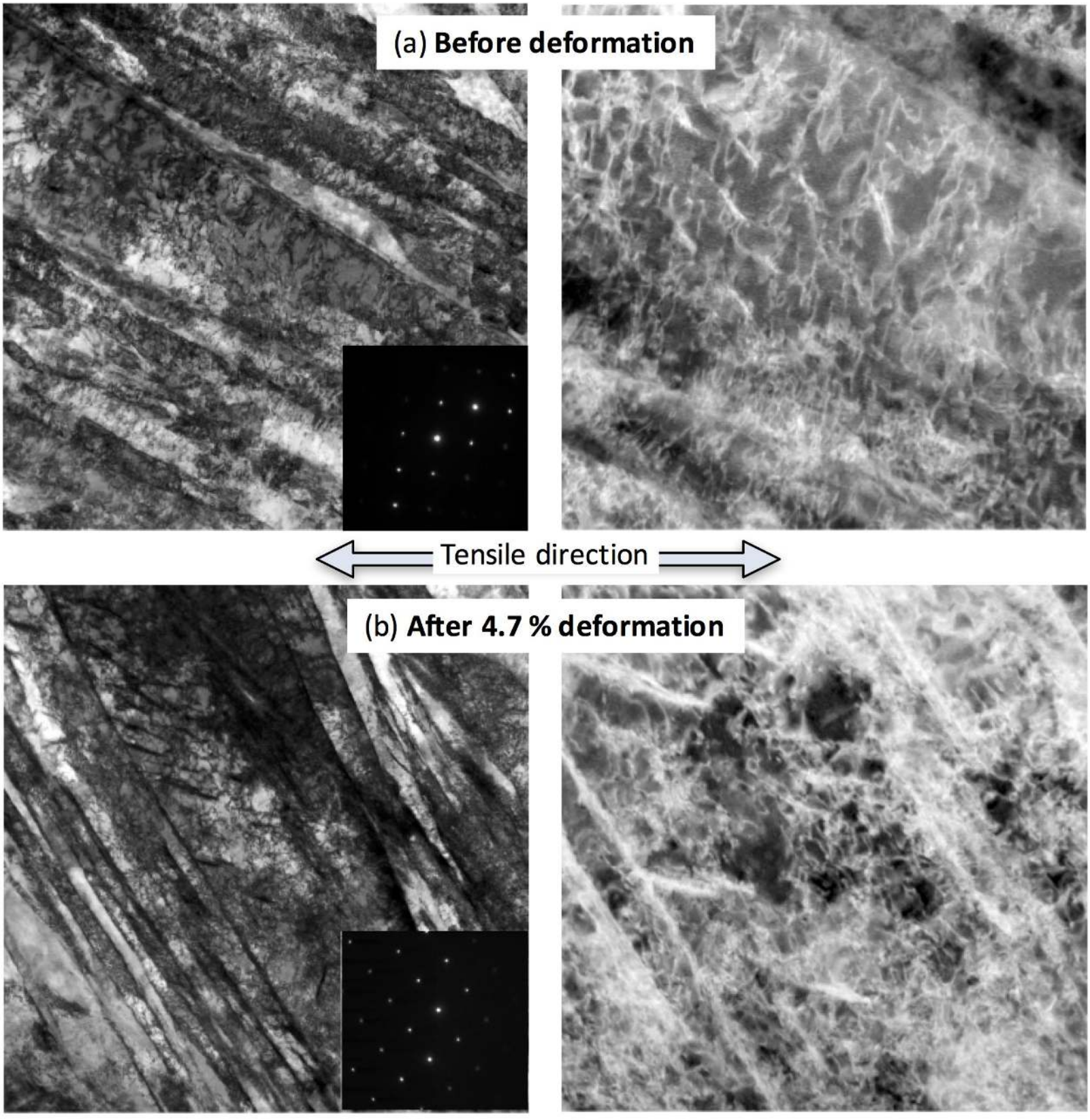
(a) Before deformation
Tensile direction
(b) After 4.7 % deformation
0.5 μm
Bright field (BF) images
200 nm
Annular dark field (ADF) images

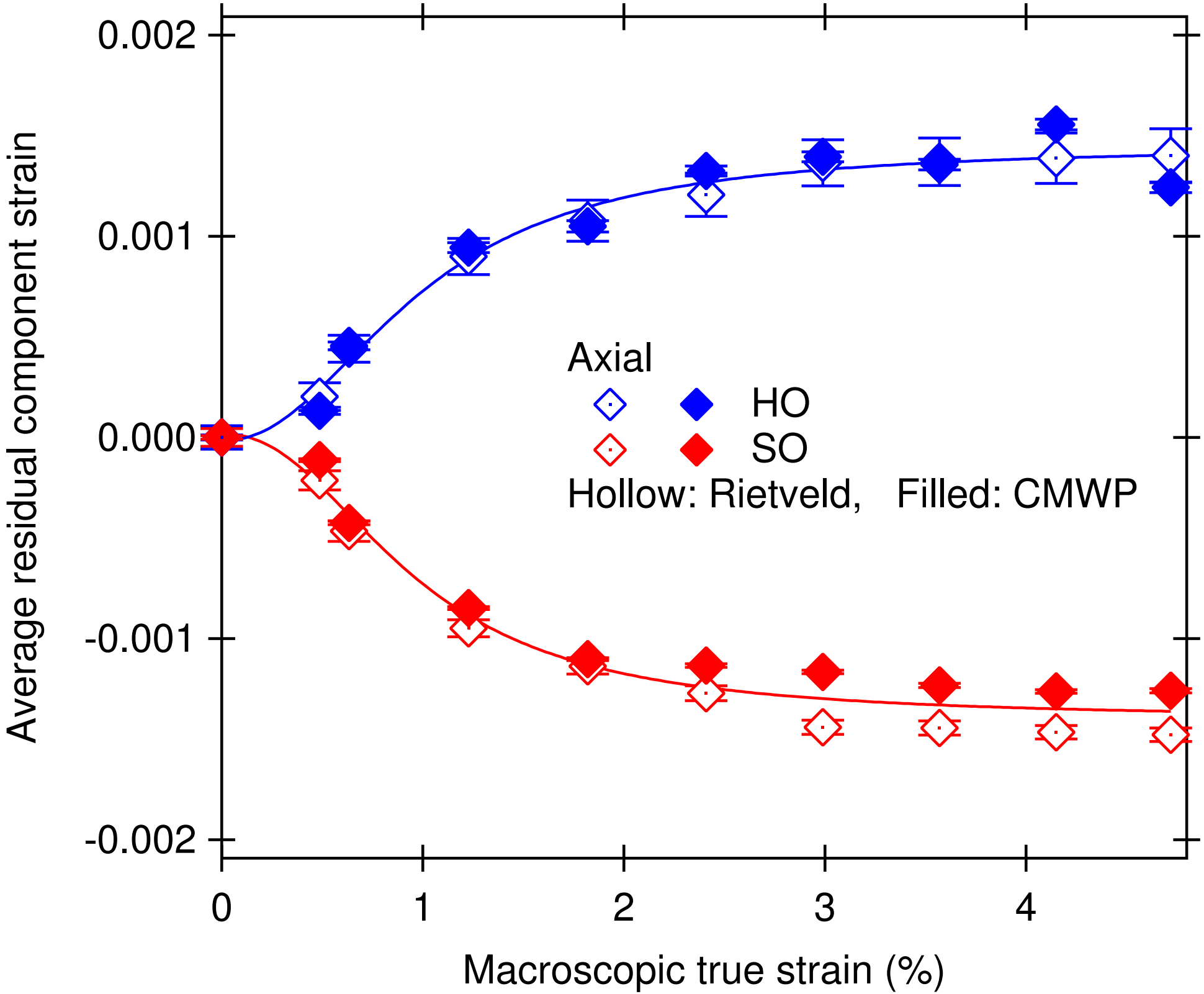
0.002
0.001
0.000
-0.001
-0.002
Average residual component strain
0
1
2
3
4
Macroscopic true strain (%)
Axial
HO
SO
Hollow: Rietveld, Filled: CMWP

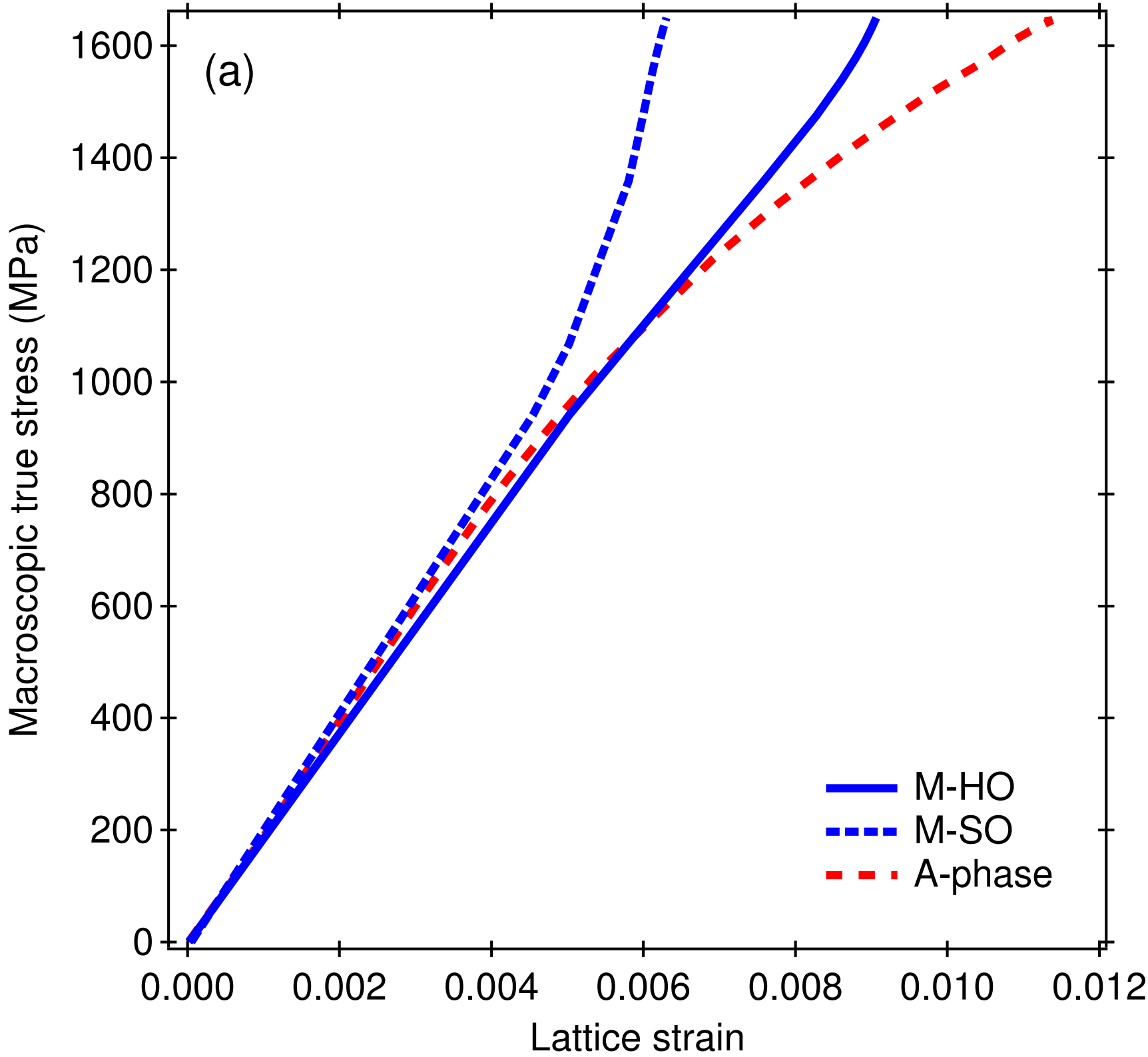
(a)
Macroscopic true stress (MPa)
Lattice strain
0
200
400
600
800
1000
1200
1400
1600
0.000
0.002
0.004
0.006
0.008
0.010
0.012
M-HO
M-SO
A-phase

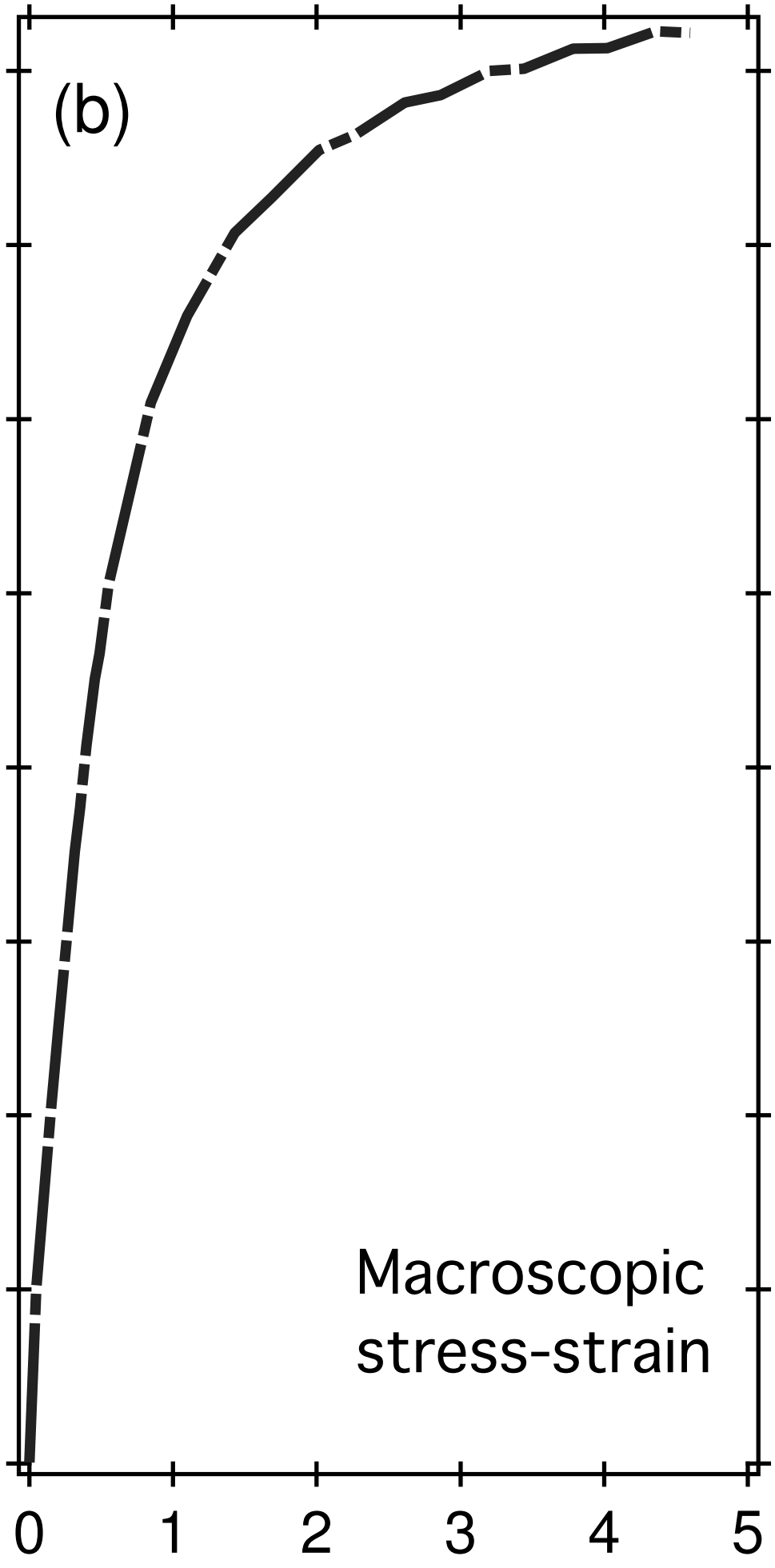
(b)
Macroscopic
stress-strain
0
1
2
3
4
5
Macroscopic true strain (%)

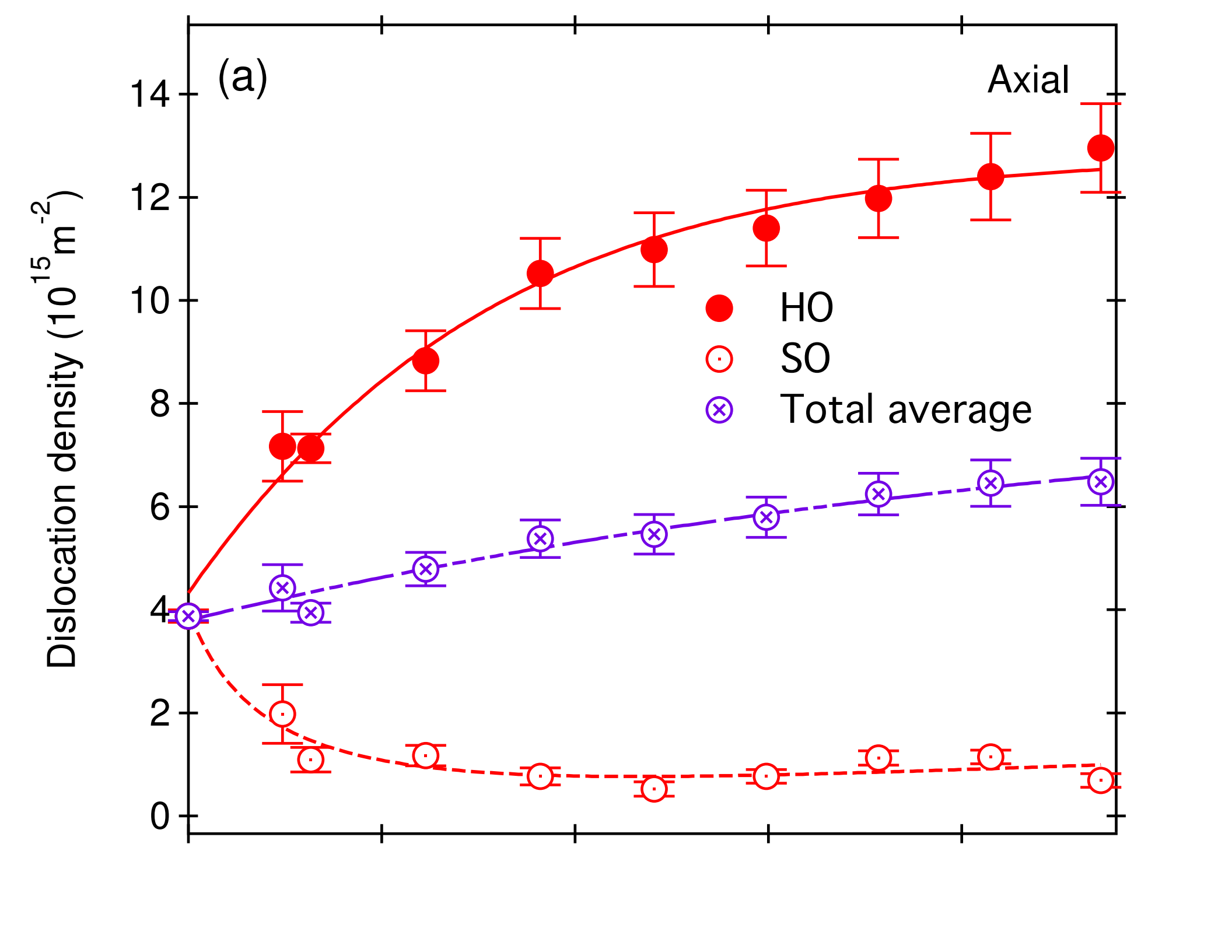
(a)
Axial
HO
SO
Total average
Dislocation density (10^{15} m^{-2})
0
2
4
6
8
10
12
14

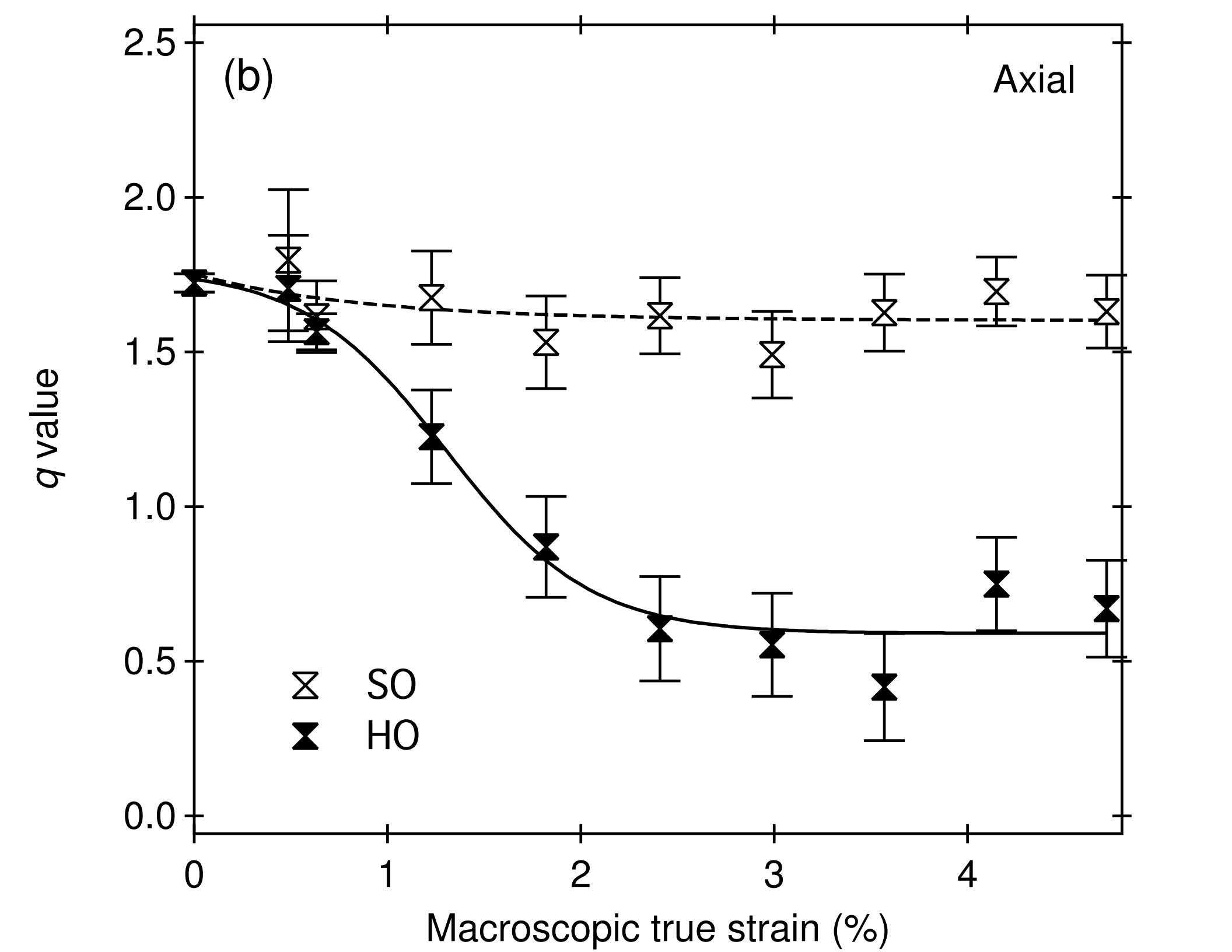
(b)
Axial
2.5
2.0
1.5
1.0
0.5
0.0
q value
SO
HO
0
1
2
3
4
Macroscopic true strain (%)

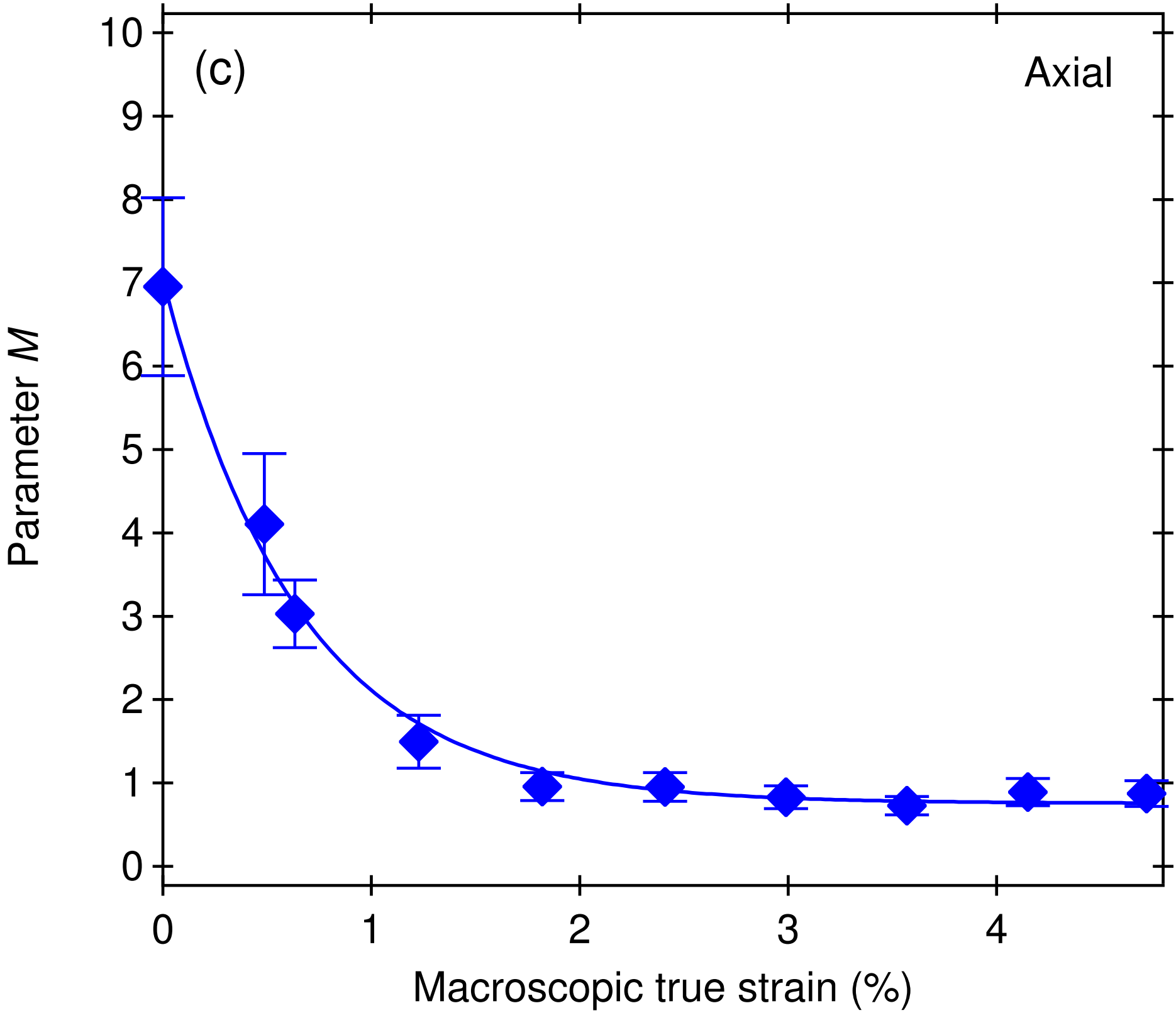
(c)
Axial
Parameter M
Macroscopic true strain (%)
0
1
2
3
4
5
6
7
8
9
10

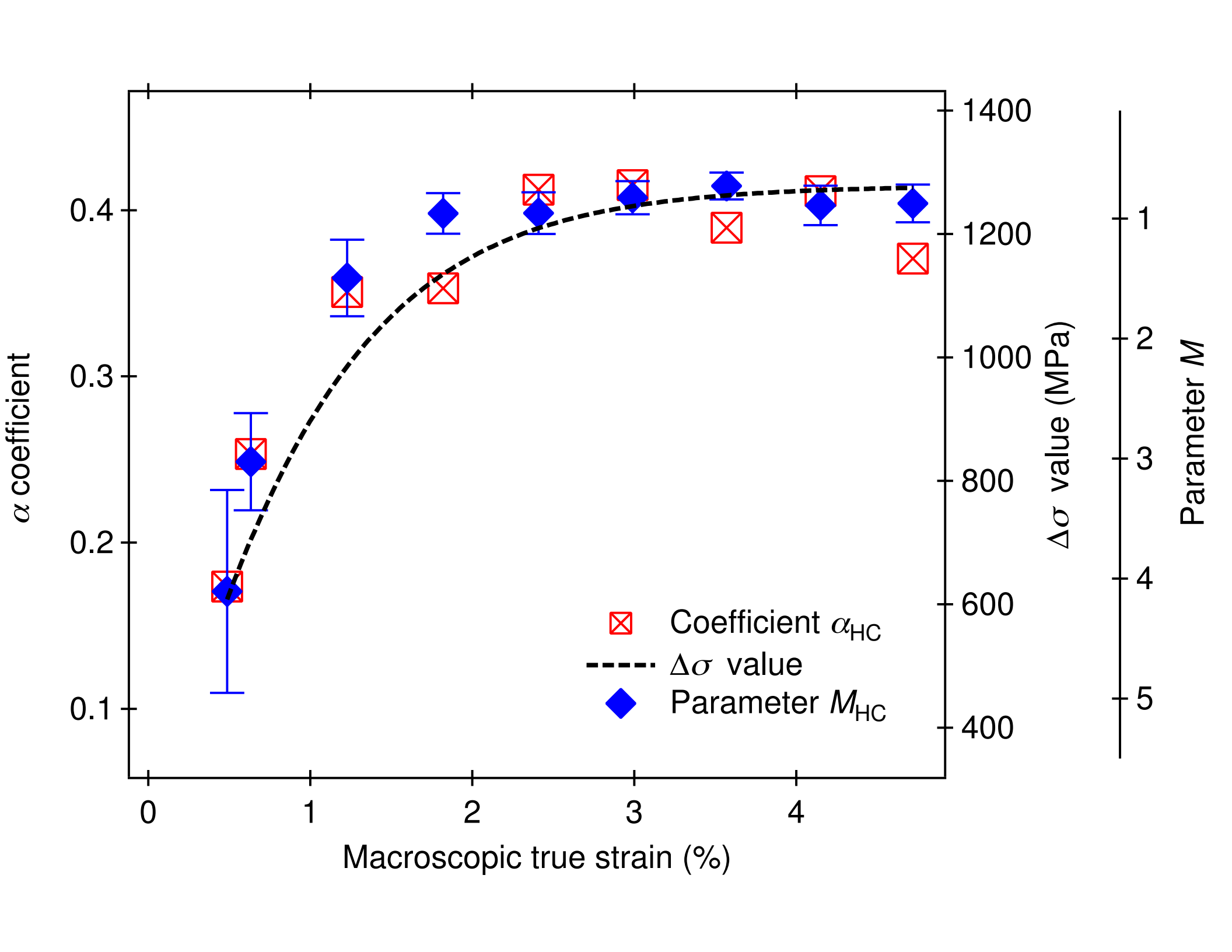
α coefficient
0.4
0.3
0.2
0.1
0
1
2
3
4
Macroscopic true strain (%)
1400
1200
1000
800
600
400
Δσ value (MPa)
1
2
3
4
5
Parameter M
Coefficient α_{HC}
Δσ value
Parameter M_{HC}